JVR
Journal of
Vascular Research

Review Article

J Vasc Res
DOI: 10.1159/000514211

Received: September 14, 2020
Accepted: December 23, 2020
Published online: April 9, 2021

Vascular Patterning as Integrative Readout of Complex Molecular and Physiological Signaling by VESsel GENeration Analysis

Mark Lagatuz[a] Ruchi J. Vyas[b] Marina Predovic[c] Shiyin Lim[c] Nicole Jacobs[c] Miguel Martinho[d] Hamed Valizadegan[d] David Kao[e] Nikunj Oza[e] Corey A. Theriot[f, g] Susana B. Zanello[g] Giovanni Taibbi[h] Gianmarco Vizzeri[h] Mariana Dupont[i] Maria B. Grant[i] Daniel J. Lindner[j] Hans-Christian Reinecker[k] Alexander Pinhas[l] Toco Y. Chui[l] Richard B. Rosen[l, m] Nicanor Moldovan[n, o] Mary B. Vickerman[p] Krishnan Radhakrishnan[q, r] Patricia Parsons-Wingerter[s, t]

[a]Redline Performance Solutions, Ames Research Center, National Aeronautics and Space Administration, Moffett Field, CA, USA; [b]Mori Associates, Space Biology Division, Ames Research Center, National Aeronautics and Space Administration, Moffett Field, CA, USA; [c]Blue Marble Space Institute of Science, Space Biology Division, Ames Research Center, National Aeronautics and Space Administration, Moffett Field, CA, USA; [d]Universities Space Research Association, Intelligent Systems Division, Exploration Technology Directorate, Ames Research Center, National Aeronautics and Space Administration, Moffett Field, CA, USA; [e]Advanced Supercomputing & Intelligent Systems Divisions, Exploration Technology Directorate, Ames Research Center, National Aeronautics and Space Administration, Moffett Field, CA, USA; [f]Department of Preventive Medicine and Community Health, The University of Texas Medical Branch at Galveston, Galveston, TX, USA; [g]KBRWyle, Johnson Space Center, National Aeronautics and Space Administration, Houston, TX, USA; [h]Department of Ophthalmology and Visual Sciences, The University of Texas Medical Branch at Galveston, Galveston, TX, USA; [i]Department of Ophthalmology and Visual Sciences, School of Medicine, University of Alabama, Birmingham, AL, USA; [j]Taussig Cancer Institute, Cleveland Clinic Foundation, Cleveland, OH, USA; [k]Departments of Medicine and Immunology, Division of Digestive and Liver Diseases, University of Texas Southwestern Medical Center, Dallas, TX, USA; [l]Department of Ophthalmology, New York Eye and Ear Infirmary of Mount Sinai, New York, NY, USA; [m]Icahn School of Medicine at Mount Sinai, New York, NY, USA; [n]Department of Ophthalmology, Indiana University School of Medicine and Indiana University-Purdue University at Indianapolis, Indianapolis, IN, USA; [o]Richard L. Roudebush VA Medical Center, Veteran's Administration, Indianapolis, IN, USA; [p]Data Systems Branch, John Glenn Research Center, National Aeronautics and Space Administration, Cleveland, OH, USA; [q]Center for Behavioral Health Statistics and Quality, Substance Abuse and Mental Health Services Administration, U.S. Department of Health and Human Services, Rockville, MD, USA; [r]College of Medicine, University of Kentucky, Lexington, KY, USA; [s]Space Biology Division, Space Technology Mission Directorate, Ames Research Center, National Aeronautics and Space Administration, Moffett Field, CA, USA; [t]Low Gravity Exploration Technology, Research and Engineering Directorate, John Glenn Research Center, National Aeronautics and Space Administration, Cleveland, OH, USA

karger@karger.com
www.karger.com/jvr

Correspondence to:
Patricia Parsons-Wingerter, patricia.a.parsons-wingerter@nasa.gov

Karger

Keywords
Microvascular · Angiogenesis · Spaceflight-Associated Neuro-ocular Syndrome · Keratinocyte growth factor · 3D bioprinting · Diabetic retinopathy · Central retinal vein occlusion · *Saccharomyces boulardii* · Leronlimab

Abstract
The molecular signaling cascades that regulate angiogenesis and microvascular remodeling are fundamental to normal development, healthy physiology, and pathologies such as inflammation and cancer. Yet quantifying such complex, fractally branching vascular patterns remains difficult. We review application of NASA's globally available, freely downloadable VESsel GENeration (VESGEN) Analysis software to numerous examples of 2D vascular trees, networks, and tree-network composites. Upon input of a binary vascular image, automated output includes informative vascular maps and quantification of parameters such as tortuosity, fractal dimension, vessel diameter, area, length, number, and branch point. Previous research has demonstrated that cytokines and therapeutics such as vascular endothelial growth factor, basic fibroblast growth factor (fibroblast growth factor-2), transforming growth factor-beta-1, and steroid triamcinolone acetonide specify unique "fingerprint" or "biomarker" vascular patterns that integrate dominant signaling with physiological response. In vivo experimental examples described here include vascular response to keratinocyte growth factor, a novel vessel tortuosity factor; angiogenic inhibition in humanized tumor xenografts by the anti-angiogenesis drug leronlimab; intestinal vascular inflammation with probiotic protection by *Saccharomyces boulardii*, and a workflow programming of vascular architecture for 3D bioprinting of regenerative tissues from 2D images. Microvascular remodeling in the human retina is described for astronaut risks in microgravity, vessel tortuosity in diabetic retinopathy, and venous occlusive disease.

Introduction

Angiogenesis, lymphangiogenesis, and other microvascular remodeling are required for the pathophysiology of diseases such as cancer, diabetes, and coronary vessel disease, as well as for the normal physiology of reproduction, embryonic development, and wound-healing [1–4]. However, the associated vascular patterns are difficult to characterize because of the fractal-based complexity of vascular trees and capillary networks. The VESsel GENeration (VESGEN) analysis software was developed to automatically generate informative maps of vascular trees, networks, and tree-network composites for calculation of major parameters such as the fractal dimension, vessel diameter, tortuosity, and various vascular densities that include vessel length and branch point. Vascular morphology can be classified into 3 basic geometric patterns: (1) asymmetric, heterogeneous trees composed of vessels that branch and taper; (2) relatively homogeneous, symmetric networks (plexuses), and (3) tree-network composites [5]. Vascular trees typically develop from immature, capillary-like vasculogenic networks. Capillary networks are necessarily continuous with the arterial and venous trees of mature tissues and organs.

The VESGEN analysis is based on physiological rules of vertebrate vascular branching that include vessel tapering, bifurcational branching, and the fluid continuum requirements of laminar blood flow. Arterial and venous trees are decomposed into branching generations for site-specific quantification of vascular change because the functions of small blood vessels, for example, are very different from those of large vessels. For capillary and vasculogenic networks, basic geometric relationships between vessel morphology and avascular spaces (AVSs) are quantified. Other vascular analysis software packages are compared to VESGEN (see online suppl. Table 1, suppl. Background; see www.karger.com/doi/10.1159/000514211 for all online suppl. material) which include REAVER [6], AutoTube [7], AngioTool [8], the retinal-specific SIVA [9], Vampire [10], Ivan [11], and a parafoveal capillary density deviation mapping customized for ocular coherence tomography (OCT)-angiography (OCT-A) [12–14]. For other physiological capabilities, VesSAP was developed to quantify 3D vascular branching in the mouse brain [15] and AngioQuant, endothelial tubes in in vitro culture [16]. AutoTube, AngioTool, and REAVER analyze parameters common to both vascular networks and trees such as branch points and vessel length density. In addition to these parameters, VESGEN analyzes vascular trees and tree-network composites by automatically assigning (classifying) vessels into specific branching generations, and includes other algorithms specific to networks. The capability for vessel generation assignment further distinguishes VESGEN from SIVA, Vampire, and Ivan, which analyze the human and primate retinas by quantifying the diameters of larger arteries and veins.

To date, all angiogenic stimulators and inhibitors analyzed by VESGEN, including vascular endothelial growth factor (VEGF), basic fibroblast growth factor (bFGF or fibroblast growth factor [FGF]-2), transforming growth

factor (TGF)-β1, angiostatin, keratinocyte growth factor (KGF or FGF-7), and drugs such as leronlimab and the steroid triamcinolone acetonide, have induced unique "fingerprint" or "signature" vascular patterns [5, 17–24]. These early experimental findings with VESGEN suggest the hypothesis that vascular patterning represents an integrative biomarker or readout of complex molecular and physiological multi-scale signaling.

In this review, the analysis of vascular trees and networks by VESGEN is illustrated by (1) retinal changes in crew members after long-duration missions to the International Space Station (ISS), (2) vessel tortuosity during early-stage progression of diabetic retinopathy (DR), (3) central retinal vein occlusion (CRVO) in the human retina, (4) inhibition of angiogenesis in humanized mouse tumors, (5) the unique vascular pattern of the epithelial activator KGF as a novel vessel tortuosity factor in an avian model, and (6) the probiotic control of gastrointestinal inflammation in a mouse model. A prototype for the 3D programming of vascular architecture from 2D images of the rat retina for bioprinting of regenerative tissues is described. How the analysis could be adapted to other fractal vascular branching systems such as vein mutations in the wings of *Drosophila melanogaster*, developing leaf venation in *Arabidopsis thaliana* [25, 26], and neuronal branching is discussed.

VESGEN Analysis Software

Description

VESGEN (version 1.10) is software developed by the US National Aeronautics and Space Administration (NASA) that is globally available and freely downloadable upon request [27]. The software provides an interactive menu-driven user interface containing 3 analysis options: *Vascular Tree*, *Vascular Network,* and *Tree-Network Composite* (online suppl. Fig. 1; online suppl. Background). Detailed explanations of the software are available in the *User Guide* and elsewhere [5]. Written in Java, VESGEN operates as a sophisticated plug-in bundled with software ImageJ v1.51r [28]. Image-processing algorithms include those from the standard ImageJ toolset and extensive customized analyses. Early results for VESGEN were generated by a semi-automated software prototype [17–19, 22]. A new capability for the automated binarization (segmentation) of grayscale vascular images for subsequent VESGEN analysis by artificial intelligence (AI)/deep learning methods will be included in v1.11, scheduled for 2021 release.

Capabilities

A user-provided vascular binary image serves as the sole input for automated software analysis. User-generated or customized region-of-interest (ROI) options are available. The output consists of specialized vascular maps, spreadsheets of numerical results, and a log documenting the analysis. Vascular output parameters include vessel diameter (D_v), vessel tortuosity (T_v), vessel area density (A_v), vessel length density (L_v), vessel number density (N_v), vessel branch point density (Br_v), end point density (E_v), and the fractal dimension (D_f, measured by a box-counting algorithm) [5, 17–19, 22, 23, 29, 30]. The space-filling properties of complex objects such as vertebrate vascular branching, arboreal trees, coastlines, and angiosperm leaves are measured by fractal mathematics, a non-Euclidean geometry developed by Mandelbrot and others [31, 32]. These objects are characterized by the geometric property of self-similarity (i.e., repetition of a pattern such as vascular bifurcational branching at increasingly smaller length scales). For 2D images, D_f varies as a fractional value between 1 and 2, the limiting Euclidean dimensions of a line and rectangle. As other examples, L_v is defined as the total vessel length divided by the area of the image or ROI. Vessel tortuosity, T_v, is calculated as the ratio of the arc length of the vessel to the chord length (i.e., the distance of the straight line connecting the 2 end points of the vessel) [33–35]. A minimum value for T_v is, therefore, 1.0. Parameters are reported in pixel units and additionally in physical units if a microscope calibration factor is entered. To optimize the results, a user can interact with the interface to select other helpful features such as recombining the branching generations into groups of small, medium, and large vessels. Mapping and quantification are based on algorithms for the vessel skeleton (centerline) and vessel area, and fractal box-counting [5, 17]. The algorithms were validated by pixel counting of the skeleton and area vessel density in ImageJ and by comparing the fractal box-counting algorithm in ImageJ with another box-counting program written in MATLAB® (The MathWorks, Inc., Natick, MA, USA).

Vascular Trees

Vascular trees are highly branching, asymmetric structures characterized by tapering vessels. For analysis of successive branching generations by the *Vascular Tree* option, vessels are assigned to the proper generation by specialized algorithms according to a repertoire of vascular branching rules (Fig. 1) [5]. The averaging of many parameters such as vessel length or diameter within a vascular tree is not generally meaningful because the pa-

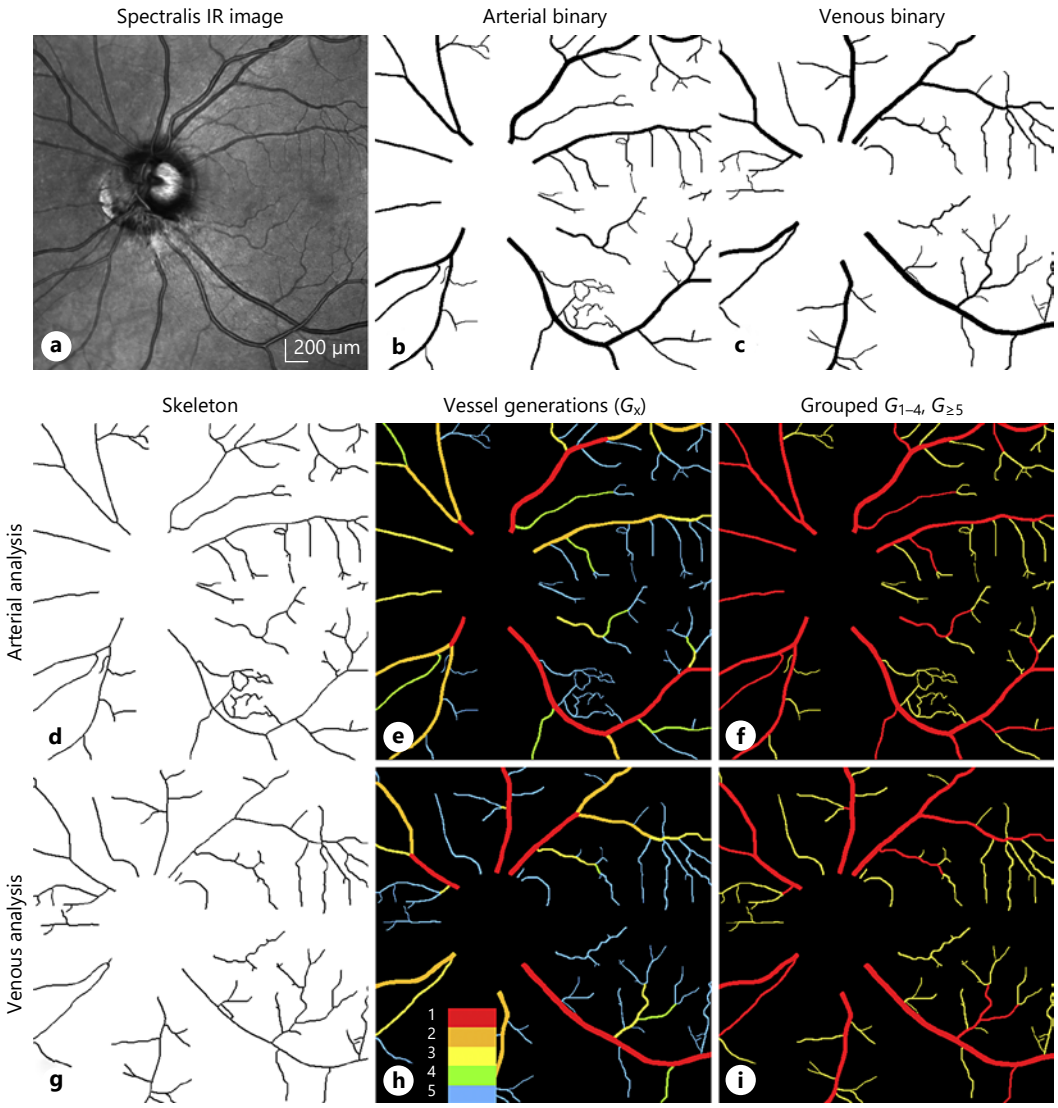

Fig. 1. Mapping and quantification by VESGEN of arterial and venous trees. The vascular tree analysis is illustrated by an image of the left retina of an astronaut crew member acquired after a 6-month mission to the ISS. Binary arterial and venous trees extracted from the grayscale image (**a–c**) served as sole inputs to the software for the automated generation of arterial and venous maps (**d–i**). The software first generates a distance map and skeleton (centerline) of the vascular branching that supports calculation of the fractal dimension (D_f) and overall vessel length density (L_v). Together the vascular binary image, distance map and skeleton then generate additional mappings such as the branching generations for calculation of site-specific information on differences in vessel parameters that include small and large vessel diameters, density, and tortuosity. For this image, arterial and venous D_f were 1.354 and 1.329 and L_v, 12.1×10^{-4} and 10.7×10^{-4} µm/µm^2. Average diameter ± SD of arteries and veins per branching generation ranged from 113.2 ± 7.1 and 125.1 ± 13.0 µm for G_1 (largest generation) to 33.8 ± 10.3 and 35.0 ± 8.9 µm for G_5 (smallest). Arterial and venous branching generations (**e**, **h**) can be grouped by a user option into groups such as large and small vessels (**f**, **i**) (Fig. 2). Scale bar, 200 µm. VESGEN, VESsel GENeration; ISS, International Space Station; IR, infrared.

rameters can vary so greatly over many successive branching generations. Vessels throughout the entire tree image are decomposed by the analysis into successively smaller branching generations (G_1, G_2, … G_x), where the largest vessel is designated G_1. Vessel assignments are determined by factors such as vessel tapering

to accommodate a range of vessel sizes within a given generation, given the variability of biological vascular branching. The primary determinant of a new birfurcational vessel generation used by VESGEN is the proportional decrease in the diameters of offspring (daughter) vessels at bifurcational branch points to 71% of the parent vessel (or as a fraction, $1/\sqrt{2}$), using a user-adjustable default tolerance factor of 15%. As examples, L_{v1-3} denotes vessel length L_v with respect to larger branching generations G_1–G_3, and N_{v6} is the vessel number density N_v for the smaller branching generation G_6. Nonetheless, the most numerous branching event in most vascular trees is the offshoot of a much smaller vessel from a larger vessel, such as a G_5 vessel from a G_2 vessel [5, 18, 19, 22, 23, 36, 37]. Physical dimensions are notated as in the following example from Figure 1, where L_v ($\mu m/\mu m^2$) = 0.00121 is denoted as 12.1×10^{-4}.

Vascular Networks

Vascular networks are defined geometrically as nonbranching, closed tubular structures that are often symmetric [5, 38]. A basic constraint of vascular network analysis is that the fractional areas of network vessels and AVSs (also lacunae or holes) must sum to 1, when normalized by the total ROI area. The 2 structure-function extremes are the highly permeable, thick "presinusoidal" capillary vessels with small AVSs in the liver compared to highly impermeable, thin capillary vessels with large AVSs constituting the blood-brain barrier, as described in an interesting study of these geometric relationships [38]. The *Vascular Network* option of VESGEN generates results that include A_v, L_v, Br_v, and D_f; histogram data of vessel diameters; the number and areas of AVSs; and their geometric relationship with the vascular network, including circularity and Gaussian statistical characteristics of the overall AVS patterning. Other software packages that analyze vascular analysis networks also measure A_v, L_v, Br_v, and sometimes D_f; the AVS analysis, however, appears unique to VESGEN.

Vascular Tree-Network Composites

Vascular tree-network composites combine the asymmetric, tapering branching of trees with the more symmetric geometry of networks. The composite image can represent a normal vascular tree that is continuous with the capillary bed, as is typical of vascular branching in every vertebrate tissue and organ. The composite could also represent either a pathological neovascularization or a transitional state of development from an immature network to a more mature tree [5]. When the *Tree-Network Composite* option of VESGEN is selected, vessel parameters are generated that include the *Vascular Tree* and *Vascular Network* outputs described above.

Extraction (Segmentation) of Binary Vascular Pattern, New AI Methods, and 3D Analysis

Vascular patterns were extracted from grayscale clinical or microscopic images and converted to binary (black/white) images using Adobe Photoshop® (San Jose, CA, USA) because of the convenient layering features, described in greater detail previously [5, 23, 36]. For earlier studies, images were segmented using ImageJ. Binary vascular patterns from the human retina were further separated into arterial and venous trees using basic principles of anatomy and physiology [36]. For example, larger vessels of arterial and venous trees were treated as originating as pairs from the optic disc for which arteries are of smaller diameter than veins. Once a vascular tree was identified as arterial or venous, the tree was followed from its origin at the optic disc to its termination at the smallest generations according to vessel connectivity, bifurcational branching, and tapering (morphological characteristics of a mature vascular tree). Vessel interpretation was decided by agreement between 2 vascular analysts, subject to final decision by the senior analyst.

Methods of vessel extraction by AI/machine learning and other computational advances are being developed by NASA for automated extraction (segmentation) of binary vascular patterns from grayscale images [39]. The prototype computer code is incorporated into VESGEN software and is scheduled for release in early 2021 (v1.11). Such AI/machine learning models require training/evaluation datasets from which they learn how to perform a given task. Extensive AI studies were performed using a DR dataset, described below, comprising 34 example cases of grayscale clinical retinal images and the binary (black/white) images of vascular pattern extracted by expert vascular analysts. The DR dataset was further augmented by 40 images from a publicly available dataset of the human retina [40]. The AI/machine learning methods are able to generalize and perform reasonably well on previously unseen images. The prototype AI/machine learning code was used to extract vascular patterns from the avian chorioallantoic membrane (CAM) for the KGF study, followed by further refinement with Photoshop® (Fig. 4). A prototype for 3D bioprinting capabilities with 3D vascular tubular patterns transformed from 2D vascular images is in early-stage development and summarized in the 3D bioprinting section below.

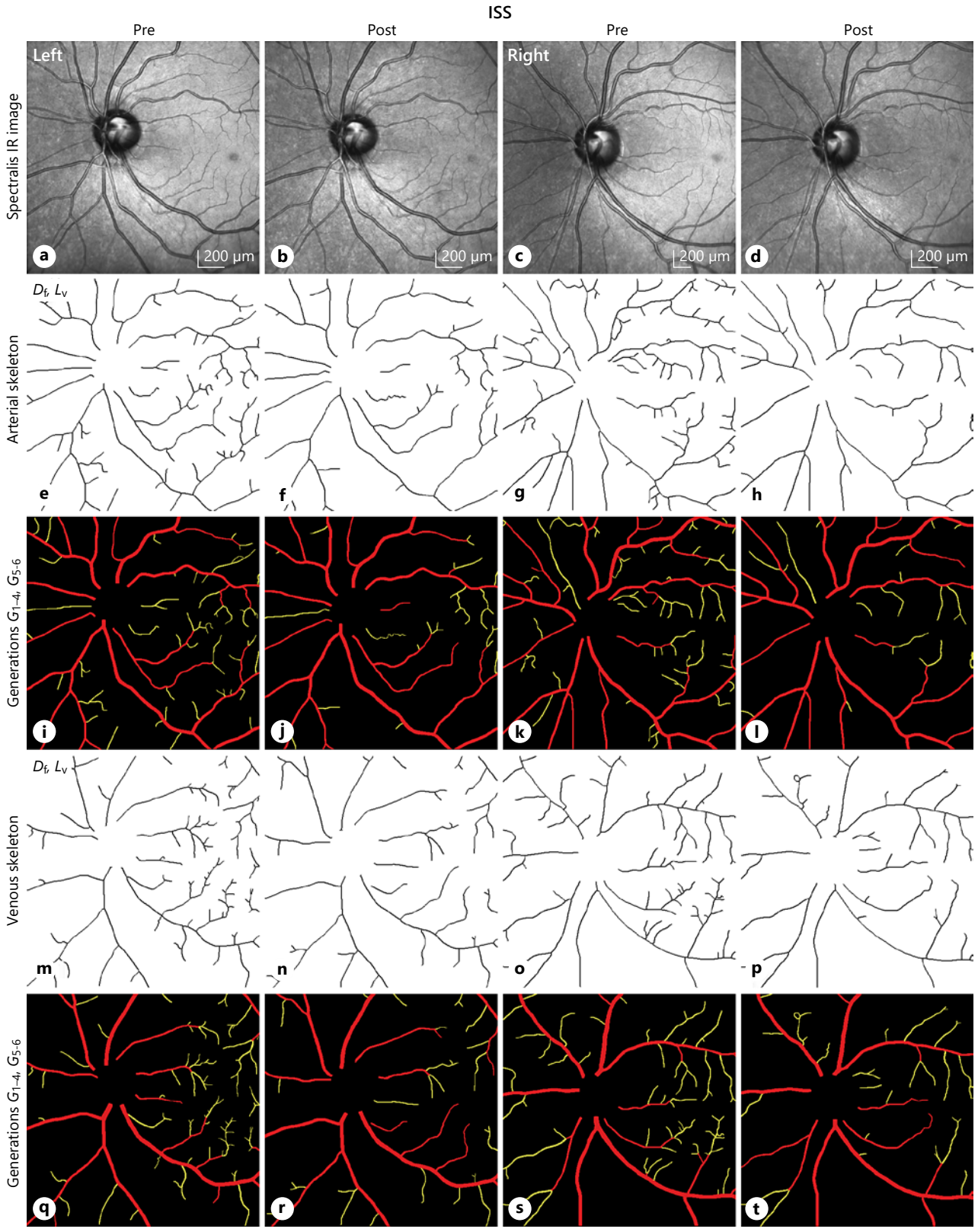

2

(For legend see next page.)

Statistical Analysis

Results of the clinical and animal in vivo studies are expressed as either mean ± standard deviation ($\bar{x}$ ± SD) or as mean ± standard error ($\bar{x}$ ± SE). Values of comparative groups were calculated using an unpaired *t* test and an a priori 2-sided significance level (*p*) of 0.05.

Vascular Trees

Vascular Decrease in the Retinas of Astronauts after Long-Duration Missions to ISS

Recent studies on the astronaut retina reveal that significant risks for ocular and visual damage are incurred by astronauts exposed to microgravity during long-duration missions on the ISS [28, 41–43]. Denoted by NASA as the spaceflight-associated neuro-ocular syndrome (SANS; formerly visual impairment and intracranial pressure syndrome), symptoms include optic disc edema, increased retinal and choroidal thickness, cotton wool spots, and decreased near visual acuity. The syndrome is believed to be associated with the headward fluid shifts that occur in microgravity. We tested the hypothesis that blood vessels in the human retina necessarily remodel in response to these physiological stressors and that the vascular changes measured by VESGEN may provide a sensitive, early-stage predictor of SANS susceptibility [30].

Following approval of the retrospective study design by the Institutional Review Board and Lifetime Surveillance of Astronaut Health (LSAH) at the NASA Johnson Space Center, 8 US astronauts were recruited for the VESGEN study with written informed consent. All astronaut crew members had completed 6-month missions aboard the ISS with pre- and postflight examinations that included OCT by Heidelberg Engineering GmbH Spectralis® (Heidelberg, Germany), with retinal vascular images centered on the optic disc acquired by 30° near infrared mode (Fig. 1, 2).

Postflight arterial and venous decreases were quantified by D_f and L_v in 11/16 retinas [30]. The losses resulted primarily from a decrease in density of small vessels. Overall, vascular decreases ranged from low to highest in the single retina diagnosed with SANS. Relative to the SANS retina, high losses in arterial and venous patterning also occurred bilaterally in another astronaut (Fig. 2; Table 1).

Currently, it is not known whether substantial postflight vascular decreases in crew member retinas resulted from vaso-obliteration (vascular dropout or loss), from decreases in the vessel diameter below the limit of image resolution, or from both. This vessel loss is likely associated with the ocular edema that is well documented for SANS and is discussed in more detail elsewhere [30]. Studies of human response to microgravity and space radiation health risks are of increasing importance, given the current global interest in lunar colonization and deep space exploration. In general, research with VESGEN has revealed that the smaller vessels remodel most actively during progressive vascular-dependent processes such as DR and molecular regulation of angiogenesis and antiangiogenesis [5, 18, 19, 22, 23, 30, 36, 37, 44, 45].

Remodeling of Arterial and Venous Trees with Progression of Diabetic Retinopathy

DR remains the leading cause of blindness of working-aged adults in industrialized countries [46]. The early stages of mild, moderate, and severe nonproliferative DR (NPDR) are defined by progressive changes in vascular status that precedes the pathologically excessive neovascularization of late-stage proliferative DR (PDR). Previous VESGEN research revealed a surprising, homeostatic-like alternation or oscillation of retinal vessel density [36]. Vessel density increased or proliferated during moderate NPDR compared to mild NPDR, prior to vascular dropout during severe NPDR and final neovascularization during PDR. We, therefore, continue to investigate DR with VESGEN for better understanding of potential approaches to reverse or stop early-stage progression. For example, as demonstrated by various lines of evidence, activation of the vasoprotective arm of the renin-angiotensin system within hematopoietic stem/progenitor cells may offer a promising early-stage strat-

Fig. 2. Vascular decrease in the retinas of an astronaut after 6 months on the ISS. Arterial and venous density decreased in the left and right postflight retinas of an astronaut crew member. Binary arterial and venous trees extracted from grayscale images of the left and right retinas (**a–d**) were analyzed by VESGEN as vascular skeletons (**e–h**, **m–p**) and generational branching grouped into large (G_{v1-4}, red) and small (G_{v5-6}, yellow) generations (**i–l**, **q–t**). Decreases in vascular parameters were calculated from skeletonized and grouped maps (Table 1). For visual comparison, all images were aligned with the ON to the left (i.e., images of the right retina rotated 180°). Scale bar, 200 µm. VESGEN, VESsel GENeration; ISS, International Space Station; ON, optic nerve; IR, infrared.

Table 1. Decreased vascular patterning in the retinas of an astronaut after 6-month mission on the ISS

Vascular tree	Parameter	Symbol	Left, preflight	Left, postflight	Right, preflight	Right, postflight
Arterial	Fractal dimension	D_f	1.355	1.310	1.367	1.316
	Length density					
	All vessels	L_v	12.33	9.94	12.98	10.16
	Large vessels	L_{v1-4}	7.90	7.71	8.36	7.84
	Small vessels	$L_{v\geq5}$	4.43	2.23	4.62	2.29
Venous	Fractal dimension	D_f	1.326	1.284	1.332	1.290
	Length density					
	All vessels	L_v	10.53	8.64	10.81	9.02
	Large vessels	L_{v1-4}	5.64	5.86	5.08	5.73
	Small vessels	$L_{v\geq5}$	4.89	2.82	5.58	3.47

Arterial and venous densities from the skeletonized (linearized) and grouped generation maps of the left and right retinas of an astronaut (Fig. 2) were quantified by VESGEN with 2 confirming measures, D_f and parameters for L_v. D_f, fractal dimension (dimensionless); L_v, vessel length density. Physical dimensions of L_v, L_{v1-4}, $L_{v\geq5}$, $\times10^{-4}$ μm/μm^2. VESGEN, VESsel GENeration; ISS, International Space Station.

egy for prevention or reversal of early-stage progression during NPDR [47–50].

Following approval of the University of Florida Institutional Review Board, 39 diabetic patients at varying stages of DR ranging from mild to moderate or severe NPDR, as well as 39 age- and sex-matched healthy controls, were recruited with written informed consent (detailed report in progress). Retinas of the subjects were photographed at 12.5 μm/pixel by 30° Heidelberg Spectralis® OCT following fluorescein angiography (FA) according to standards of the Early Treatment Diabetic Retinopathy Study (ETDRS).

Early results of the current larger DR study show that arterial and venous densities, particularly of the small vessels, increased with NPDR progression (Fig. 3; Table 2). Note that with the increased resolution of OCT-FA (Fig. 3), compared to the Spectralis infrared imaging of astronauts (Fig. 1, 2), an additional 2 generations of smaller vessels were detected (G_1–G_7 compared to G_1–G_5). Of the images analyzed for this study, approximately 13% display the additional phenotype of pronounced vessel tortuosity, particularly of veins. In this and previous VESGEN studies, the overall vessel tortuosity index (T_v), a sensitive indicator, typically ranges for most vascular retinal images from approximately 1.11 to 1.15. For the tortuous arteries and veins in the NPDR retina (Fig. 3d), T_v is 1.18 and 1.19, respectively. Retinal vascular tortuosity is associated with numerous vascular-dependent diseases such as systemic hypertension, DR, and retinopathy of prematurity [34, 51]. Development of vascular tortuosity in the retina is believed to result from multiple interactive processes such as angiogenesis, changes in blood flow and blood pressure, genetic factors, and vascular degeneration. Retinal tortuosity may represent or predict similar microvascular changes occurring elsewhere in the body, such as in the brain [35].

Software developed for measuring changes with progression of DR and cardiovascular disease (or hypertension) manifesting specifically in the larger retinal vessels include SIVA [9], Vampire [10], and Ivan [11] that analyze vascular branching in color fundus images, which are of lower resolution than FA but more globally available. The analysis is based on the Knudtson-Parr-Hubbard formula for measuring retinal vessel caliber (diameter) equivalents, termed central retinal artery equivalent (CRAE) and central retinal vein equivalent (CRVE). Measurements are obtained by a geometric approach that averages the CRAE and CRVE of larger vessels radiating from the optic nerve within concentric circles centered on the optic nerve, based on the tapering properties of these vessels. The analyses combine semi-automated image-processing algorithms that first extract the binary vascular pattern, followed by some manual processing and grading. Recently, SIVA was updated with new AI/deep learning algorithms to automatically segment binary vascular patterns and generate more accurate mea-

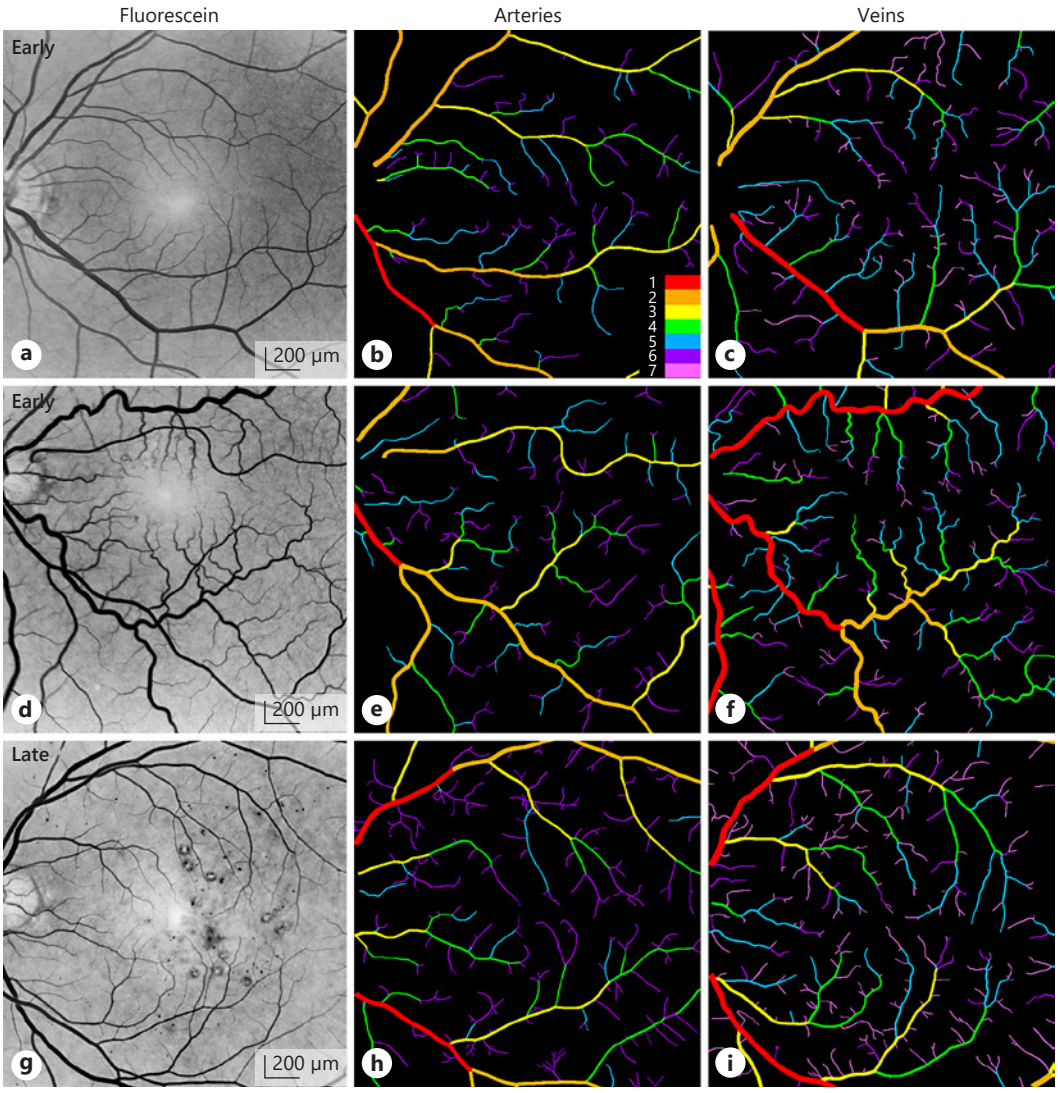

Fig. 3. Remodeling of arterial and venous trees with progression of NPDR. Clinical images of the human retina diagnosed as early (**a**, **d**) to later (**g**) stages of NPDR by the increasing presence of established clinical disease markers such as micro-aneurysms and hemorrhagic leakage. One image (**d**) is representative of a subset of retinas within the study displaying the additional phenotype of unusually tortuous vessels (approximately 13%, Table 2). Arterial (**b**, **e**, **h**) and venous (**c**, **f**, **i**) maps generated by VESGEN illustrate branching generations from G_1 to G_7 (legend). The generational maps were grouped into large (G_{1-4}) and small ($G_{\geq 5}$) generations to further quantify site-specific changes within the complex branching trees using the VESGEN generation grouping feature (Table 2). Scale bar, 200 μm. NPDR, nonproliferative diabetic retinopathy; VESGEN, VESsel GENeration.

sures than the previous semi-automated methods [9]. Healthy and cognitively impaired individuals were distinguished by the larger venular asymmetry factor and D_f of SIVA [52]. Results obtained by these software packages, although useful, differ from those generated by the VESGEN tree analyses that focus on site-specific adaptations within complex branching vascular trees. Results generated by the SIVA multifractal analysis may overlap somewhat with the VESGEN multi-generational vascular analysis.

Table 2. Progression of NPDR in arterial and venous trees of the human retina

Vascular tree	Parameter	Symbol	Mild NPDR (Fig. 3a)	Mild NPDR (Fig. 3d)	Moderate NPDR (Fig. 3g)
Arterial	Fractal dimension	D_f	1.320	1.333	1.377
	Length density				
	All vessels	L_v	1.571	1.650	2.100
	Large vessels	L_{v1-4}	0.885	0.733	0.854
	Small vessels	$L_{v\geq5}$	0.686	0.916	1.245
	Tortuosity				
	All vessels	T_v	1.150	1.190	1.130
	Large vessels	T_{v1-4}	1.124	1.149	1.109
	Small vessels	$T_{v\geq5}$	1.186	1.227	1.145
Venous	Fractal dimension	D_f	1.363	1.383	1.399
	Length density				
	All vessels	L_v	1.947	2.129	2.332
	Large vessels	L_{v1-4}	0.577	0.883	0.702
	Small vessels	$L_{v\geq5}$	1.370	1.246	1.633
	Tortuosity				
	All vessels	T_v	1.153	1.184	1.153
	Large vessels	T_{v1-4}	1.100	1.191	1.138
	Small vessels	$T_{v\geq5}$	1.177	1.180	1.159

Arterial and venous densities are quantified by VESGEN from maps of 3 human subjects diagnosed with early to later NPDR (Fig. 3) by the fractal dimension (D_f) and vessel length density (L_v). Site-specific differences are further characterized for branching generations 1 to 4 (L_{v1-4}) and generations greater than or equal to 5 ($L_{v\geq5}$). Tortuous vessels in one image (Fig. 3d) characteristic of a subset of retinas are compared to other images by a sensitive measure of vessel tortuosity (T_v), geometrically constrained as ≥1.0. Physical dimensions of L_v, L_{v1-4}, $L_{v\geq5}$, $\times10^{-2}$ px/px^2 and T_v, pixel/pixel; D_f, dimensionless. NPDR, nonproliferative diabetic retinopathy; VESGEN, VESsel GENeration.

Epithelial Activator KGF as Novel Vessel Tortuosity Factor

Produced throughout the body by mesenchymal cells such as fibroblasts, KGF is a paracrine activator of proliferation and migration via FGF receptor isoforms in the epithelium, but not endothelium [53]. Described initially as a mitogen for keratinocytes in wound healing, KGF has further demonstrated cytoprotective properties by promotion of intestinal repair [53], suppression of malignant epithelial phenotypes [54], and as a therapy, protection against radiologic, chemotherapeutic, and cytotoxic agents [55]. On the other hand, KGF and its interactions with VEGF and TGF-β2 have been implicated in the progression of choroidal neovascularization (CNV) [56]. CNV, a major cause of vision loss, is the growth of new blood vessels from the underlying choroid into the subretinal pigment epithelium via a break in Bruch's membrane. In human pancreatic ductal epithelial cells, activation by KGF of the pro-inflammatory transcription factor family, nuclear factor kappa, further stimulated the expression of VEGF and matrix metalloprotease (MMP)-9, member of a protease family involved in the degradation of the extracellular matrix [57].

In a developmental model of angiogenesis in the avian CAM, KGF strongly increased arterial tortuosity, accompanied by some increase in arterial density (Fig. 4; Table 3). In a series of 4 experiments, fertilized eggs of Japanese quail (*Coturnix coturnix japonica*) were cracked on embryonic day 3 and cultured further in 6-well petri dishes in a tissue culture incubator, as reported previously [5, 17–19, 21–23]. On E7, 0.5 mL PBS containing 10 μg of recombinant human KGF [58] was applied to the CAM surface. The CAMs were aldehyde-fixed and dissected after incubation for 48 h. Results reported here for 2 images acquired by bright-field microscopy are representative of vascular response at 2.5–20 μg KGF/CAM following 24 or 48 h of incubation. The images of end points in the arterial tree were separated from the venous tree and

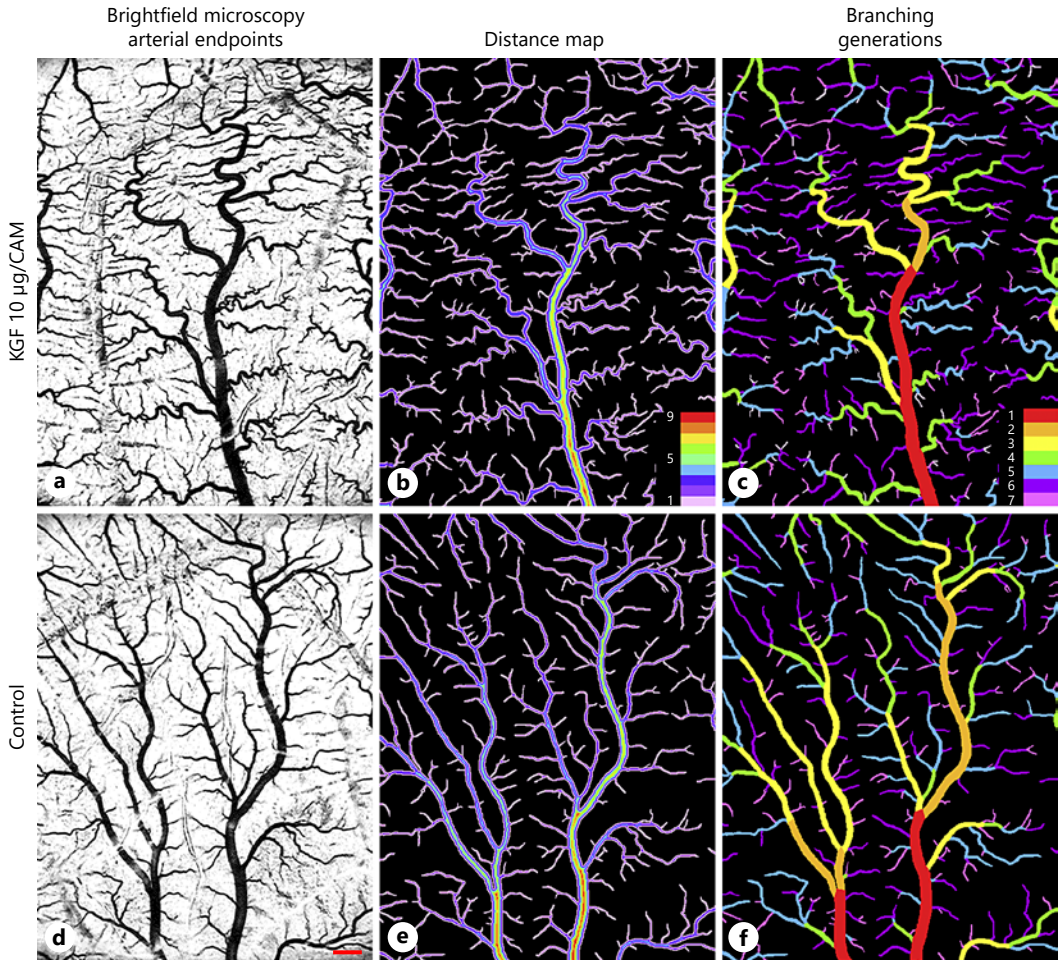

Fig. 4. Epithelial activator KGF induces vessel tortuosity in vivo. The quail CAM, avian analog of the placenta, was treated with (**a**) and without (**d**) KGF at 10 µg CAM for 48 h. Images generated by VESGEN of the arterial end points include distance maps (**b**, **e**) where legend indicates the pixel distance to the vessel edge and branching generations with legend (G_1–G_7; **c**, **f**) that support quantification of specific generational changes exerted by KGF (Table 3). As a novel regulator of vessel tortuosity, KGF may have increased the activity of MMPs in the chorionic epithelium [57], thereby decreasing tissue resistance to sinusoidal vascular patterning by the pulsatile blood flow. Scale bar, 500 µm (**d**). VESGEN, VESsel GENeration; KGF, keratinocyte growth factor; CAM, chorioallantoic membrane; MMP, matrix metalloprotease.

binarized for VESGEN analysis by a well-established artifact of CAM fixation, in which blood is retained primarily within arteries but not within veins.

To our knowledge, this is the first report of KGF as a regulator of vessel tortuosity. Interestingly, in both the tortuous NPDR retina (Fig. 3d–f) and this KGF-treated developmental model, the quasi-sinusoidal pattern of the larger vessels is repeated by the small vessels at a smaller scale of decreasing amplitude and periodicity. The fractally scaling pattern, therefore, appears to be a function of the vessel diameter and is perhaps determined by the cycling pressures resulting from cardiovascular (Womersley) fluid dynamics of pulsatile blood flow. Signaling by the epithelial activator KGF to MMP's may have reduced the stiffness of the chorionic epithelium surrounding the blood vessels, allowing the sinusoidal-like curvature of the vasculature to be remodeled by pulsatile flow. Whether KGF is involved in the signaling of the subset of NPDR patients displaying significant vessel tortuosity (Fig. 3) is currently not known.

Table 3. KGF as regulator of vessel tortuosity

Parameter	Symbol	Control	KGF, 10 μg/CAM
Fractal dimension	D_f	1.463	1.506
Length density			
All vessels	L_v	3.866	4.515
Large vessels	L_{v1}	0.113	0.123
Medium vessels	L_{v2-5}	2.081	1.718
Small vessels	$L_{v\geq6}$	1.602	2.621
Tortuosity			
All vessels	T_v	1.150	1.205
Large vessels	T_{v1}	1.104	1.109
Medium vessels	T_{v2-5}	1.154	1.288
Small vessels	$T_{v\geq6}$	1.149	1.161

Vascular patterning in the arterial end points of a quail CAM treated with KGF (10 μg) is compared to untreated control (Fig. 4). Quantification by VESGEN of the skeletonized arterial patterns includes vessel tortuosity (T_v) and 2 measures of vascular space-filling capacity, the fractal dimension (D_f) and total vessel length density (L_v). Physical dimensions of L_v, L_{v1-4}, $L_{v\geq5}$, $\times10^{-2}$ μm/μm^2; T_v and D_f, dimensionless. VESGEN, VESsel GENeration; KGF, keratinocyte growth factor; CAM, chorioallantoic membrane.

The CAM assay has been used by us and others as an analog of the retinal vascular branching pattern because of its morphological similarity to the retina. We have found the CAM to be a useful, relatively easy, optically accessible model for testing and quantifying vascular responses to numerous cytokines and therapeutics that served as the critical in vivo testbed model for developing the VESGEN *Vascular Tree* option. Because this assay does not visualize venous trees, the effects of KGF and other molecular regulators on veins is not known beyond an observational level.

Inhibition of Tumor Angiogenesis in Humanized Mouse Models

Angiogenesis is required for tumors to progress beyond 2 mm in diameter [59]. Previous studies indicated that treatment with the drug leronlimab, a humanized monoclonal anti-CCR5 antibody against CCR5, abrogated xenogenic graft-versus-host disease (GVHD) in NOD *scid* IL-2 receptor gamma (NSG) mice [60]. The CCR5 receptor, a G protein-coupled integral membrane receptor, functions as a chemokine receptor on the surface of T cells, macrophages, eosinophils, dendritic cells, and some carcinoma cells, including breast and prostate [61, 62]. Activation of CCR5 leads to endothelial cell proliferation and VEGF secretion, both characteristics of angiogenesis [63, 64]. Angiogenesis plays a key role in the initiation of GVHD [65]. Therefore, we sought to determine the effects of blocking CCR5 signaling upon development of GVHD. Leronlimab blunted the development of xGVHD but did not block engraftment of normal human leukocytes in the murine bone marrow (BM).

Twenty-four hours after 2.25 Gy whole-body X-ray irradiation, male NOD.Cg-*Prkdc*^{scid}*Il2rg*^{tm1Wjl}/SzJ, commonly known as the NSG (NSG™The Jackson Laboratory, Bar Harbor, ME, USA) knockout mice, were engrafted with human BM cells. De-identified human donor cells were obtained by backflushing filter packs utilized by the Cleveland Clinic Bone Marrow Transplant program. Fresh, nonfrozen leukocytes were purified by Ficoll-Hypaque gradient centrifugation, washed in PBS, and assessed for viability (Vi-Cell™; Beckman Coulter, Inc., Brea, CA, USA). Human BM mononuclear leukocytes were injected into the lateral tail vein (10^6 cells/mouse). Twenty-four hours later, mice were inoculated intradermally in the flanks with 2×10^6 SW480 human colon carcinoma cells (ATCC, Manassas, VA, USA). On the next day, the mice were randomized into control and treatment groups of 8 animals each by body weight. Leronlimab (CytoDyn, Inc., Vancouver, WA, USA) or normal human IgG was administered intraperitoneally at 2.0 mg/mouse twice weekly.

Blood vessels growing at the periphery of dermally inoculated day 10 SW480 colon carcinoma tumors in humanized NSG™ mice were photographed using a dissecting microscope at ×12.5 magnification. Two measurements were taken to assess the tumor area (the largest diameter coplanar with the skin and a second diameter perpendicular to the first). The product of these 2 measurements was used as an index of the tumor area. Tumor photographs were subjected to digital analysis using VESGEN software, where the ROI representing the tumor mass defined the perimeter of the tumor. The output was a series of colored vessel generation maps (colored vessels

Fig. 5. Inhibition of tumor angiogenesis in a humanized mouse model. Immuno-incompetent mice (NSG™) were humanized by inoculation with normal human BM-derived leukocytes. Thereafter, SW480 human colon carcinoma cells were injected intradermally in the mouse flanks. Mice were treated either with normal human IgG (left columns) or leronlimab (right columns) at a dose of 2 mg/kg i.p. twice weekly. On day 10, the mice were euthanized, and the tumor inoculation site was photographed and subjected to VESGEN analysis. Vessel area density (A_v), pixel^2/pixel^2; vessel length density (L_v), pixel/pixel^2. VESGEN, VESsel GENeration; BM, bone marrow; NSG, NOD *scid* IL-2 receptor gamma knockout; i.p., intraperitoneally.

(For figure see next page.)

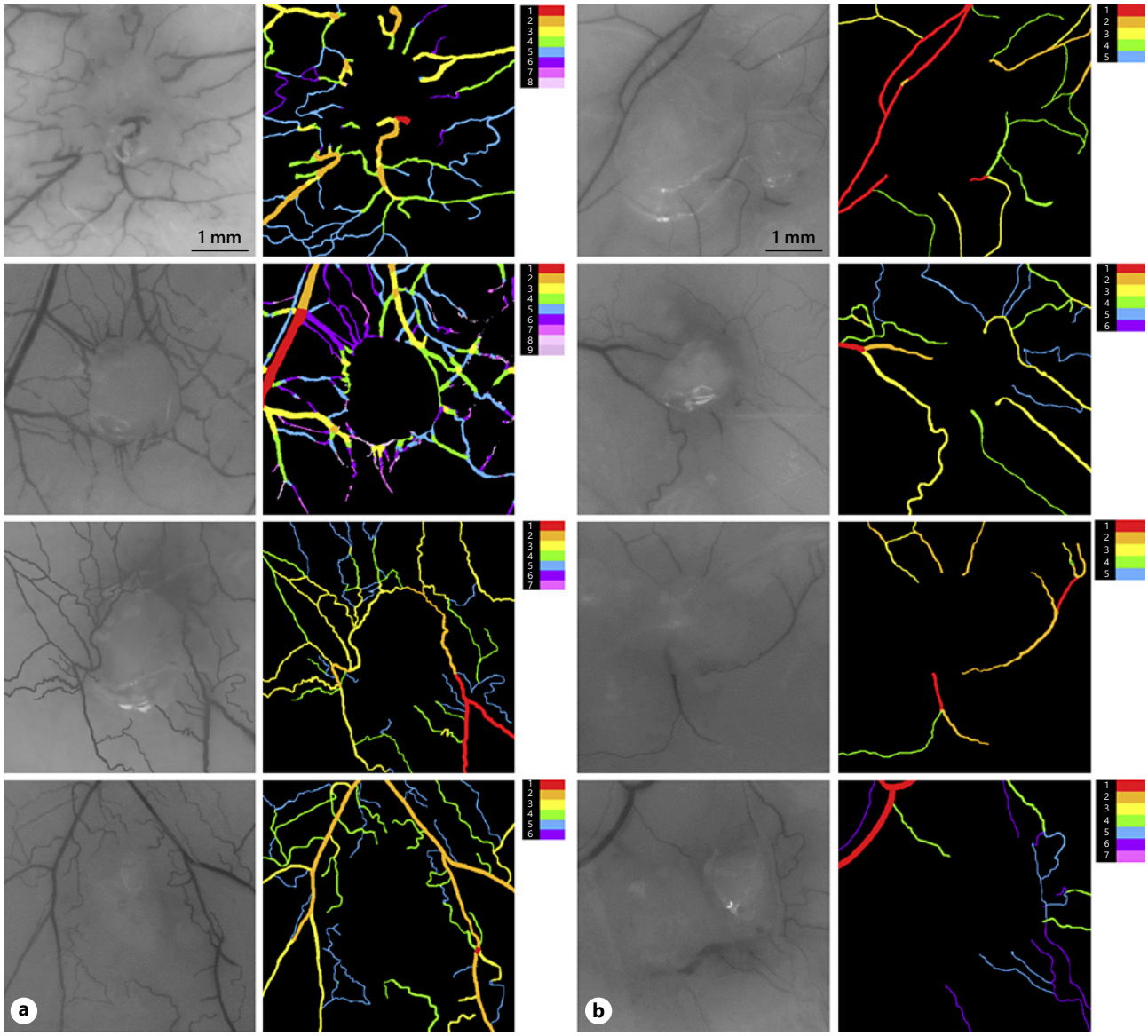
1 mm
1 mm
a
b
c
Total vessel area (pixels) mean ± SE
100,000
80,000
60,000
40,000
20,000
0
p = 0.013
IgG
Ler
Vessel length density mean ± SE
0.020
0.015
0.010
0.005
0
p = 0.0011
IgG
Ler
No. of vessels mean ± SE
80
60
40
20
0
IgG
Ler
p = 0.0082
p = 0.017
G1–G3 largest
G4–G9 smallest
Tumor area mean ± SE
3
2
1
0
p = 0.91
IgG
Ler

5

on black background, Fig. 5) in which the vessels with largest diameter were defined as G_1 (red), with each subsequent smaller generation represented as G_2–G_9. From these maps, the software calculated the total vessel area, vessel length density, vessel number, and vessel diameter.

Analysis by VESGEN at the periphery of day 10 SW480 colon carcinoma tumors inoculated in the dermis of the flanks revealed significantly fewer blood vessels in tumors from leronlimab-treated humanized mice than IgG-treated hosts (Fig. 5), consistent with leronlimab causing an inhibitory effect on neo-angiogenesis in the tumor bed. Utilization of VESGEN software allowed detailed comparisons between the 2 treatment groups and revealed marked reduction in the leronlimab-treated mice of key parameters of the vascular network feeding the tumor, including 62% reduction in the total vessel area ($p = 0.013$), 53% reduction in vessel length density ($p = 0.0011$), 61% reduction in the number of large vessels ($G_{1–3}$, $p = 0.0082$), and 80% reduction in the number of small vessels ($G_{4–9}$, $p = 0.017$). Thus, we can conclude that primary tumors from animals with the same initial tumor burden exhibited less angiogenesis following treatment with leronlimab than the controls.

Vascular Networks

Probiotic Protection in a Mouse Model of Intestinal Inflammation

Angiogenesis is required for the complex responses of inflammatory bowel diseases and for intestinal mucosal remodeling during recovery [66, 67]. In the mouse, dextran sulfate sodium (DSS) leads to a reversible colitis characterized by inflammation and angiogenesis [68, 69]. Therefore the model was used to study the effects of *Saccharomyces boulardii* (*S. boulardii*), a probiotic yeast, on remodeling of the colonic capillary vasculature during colitis induction [45]. The yeast protects against inflammatory bowel diseases, diarrhea, tumor formation, and intestinal injury by multiple immunological mechanisms [70, 71]. Nonetheless, regulation of protective mucosal host responses by *S. boulardii* is not yet fully understood. The purpose of this previously reported study [45] was to investigate how the probiotic alters signaling by VEGF receptors as fundamental regulators of angiogenesis by a combination of molecular/biological, histological, and morphological techniques that included the VESGEN *Vascular Network* analysis.

The luminal microvasculature of the normal intestine is organized as a highly regular lattice or network comprising subepithelial capillaries surrounding the mucosal glands (Fig. 6) [72]. Closed colonic vessels that appear "open" or blind-ended in 2D images actually turn into the *z*-plane to connect arterioles and venules with the underlying crypt circulation, resulting in some unconnected areas (Fig. 6) of the otherwise regular lattice spacing of the enclosed AVSs. The colonic capillaries are of small caliber (diameter) relative to the surrounding tissue and, therefore, have a small fractional ratio of the vessel area compared to the total area (i.e., total vascular plus avascular areas), unlike the large sinusoidal capillaries of the liver and lung vascular networks [5, 38]. Mapping and quantification of vascular networks by VESGEN exclude any AVSs located at the edge of the image because representation of an AVS is incomplete in those regions and its vascular density, therefore, is unknown.

To illustrate the vascular network analysis, unpublished images of the luminal capillary network in the mouse colon acquired for the previously reported study [45] were mapped and quantified with the *Vascular Network* option. In brief, 8-week-old female C57BL6 mice received 4% DSS for 5 days. Administration of *S. boulardii* was by daily oral gavage at 6×10^8 CFU. Thereafter, blood vessels were labeled by retro-orbital injection of fluorescein isothiocyanate prior to sacrifice of mice. Colon tissues were immediately removed and imaged by confocal microscopy, from which the 3D image reconstructions acquired to assess blood vessel volume and density were reduced to 2D grayscale images and binarized to black-and-white vascular patterns ($n = 5$). For the VESGEN analysis, isolated cells and (infrequent) small vessel fragments were deleted so that only connected vascular networks remained.

The highly regular lattice network of luminal capillaries in the normal mouse colon was disrupted by inflammation and angiogenesis following DSS administration (Fig. 6). Compared to control mice, the vascular inflammatory phenotype displayed statistically significant increases in vessel branch points, end points, fractional vascular area, and numbers of AVSs (holes), as reported previously (all $p < 0.05$) [45]. In addition, the mean area per AVS decreased and varied considerably in size as in the representative, previously unpublished images shown here (Fig. 6; Table 4). Although the vessel diameter increased with DSS administration, differences were not statistically significant. Treatment with *S. boulardii* (DSS + Sb, Fig. 6) considerably restored network uniformity as demonstrated by reduced variation in AVS size.

To demonstrate association with other inflammatory measures, moderation of the DSS inflammatory angiogenic response by *S. boulardii* was accompanied by reduced histologic scores of mouse colonic inflammation

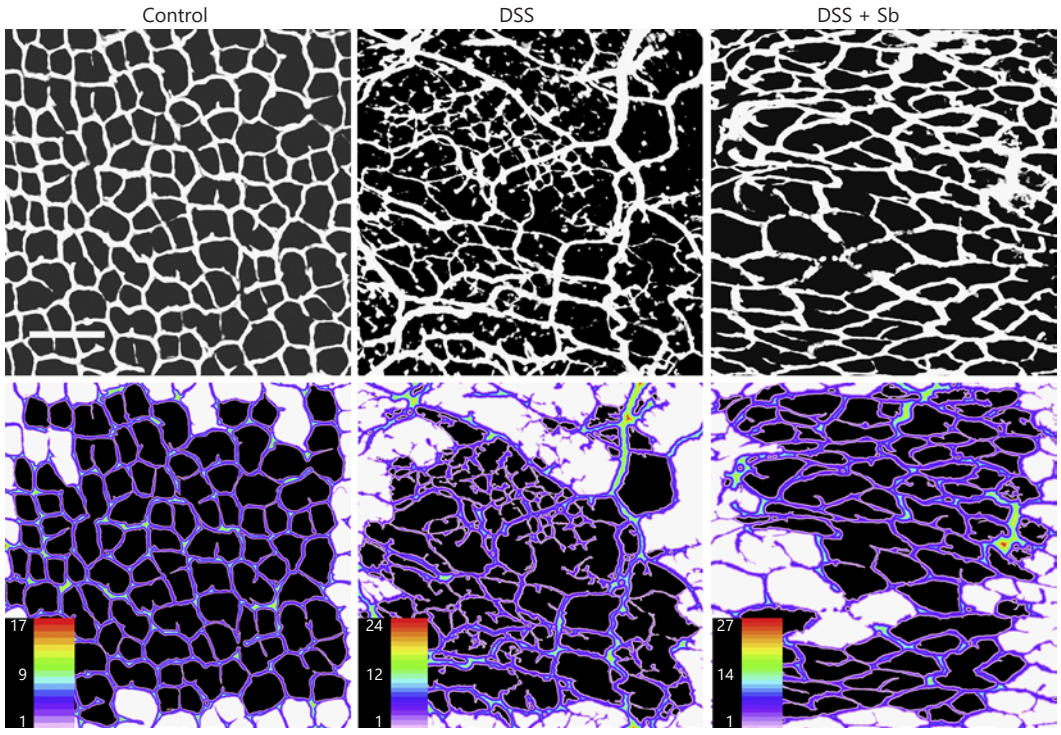

Fig. 6. Network analysis of pathological angiogenesis with probiotic protection during intestinal inflammation (first row). In confocal fluorescent images, the luminal capillary network of the normal mouse colon appears as a regular lattice structure (left column) that is disrupted by inflammation following administration of DSS (middle column). Treatment with *S. boulardii*, a yeast probiotic (right column), moderated the inflammatory angiogenic response (second row). Binary vascular patterns extracted from confocal images were mapped and quantified by VESGEN, as described previously with the *Vascular Network* option [45], in which the entire vascular pattern is analyzed for vessel parameters and fractional vascular/total areas (Table 4). However, only regions containing complete AVS (black) are quantified for other network parameters. Scale bar, 300 μm. VESGEN, VESsel GENeration; AVS, avascular space; DSS, dextran sulfate sodium.

Table 4. Inflammation and abnormal angiogenesis in the microvascular network of mouse intestine

Analysis	Groups	Control	DSS	DSS + Sb
Entire image	Vessel diameter, D_v (μm)	16.6±5.4	17.5±9.5	19.2±8.9
	Number of branch points, *Br*	304	713	425
	Number of end points, *E*	132	432	222
	Fractional vascular area, A_v	0.270	0.349	0.349
	Fractional avascular area, *A*	0.730	0.651	0.651
Enclosed AVSs	Number of AVS	90	163	115
	Area per AVS, μm^2	11,207±7,444	4,376±9,669	6,395±8,182

Results were calculated by VESGEN for either the entire image or fully enclosed AVS from Figure 6. Disruption by the DSS model of intestinal inflammation is compared to normal vascular networks and probiotic protection by *Saccharomyces boulardii*. Results expressed as mean ± SD according to microscope calibration factor, 1.48 μm/pixel. VESGEN, VESsel GENeration; AVS, avascular space; DSS, dextran sulfate sodium.

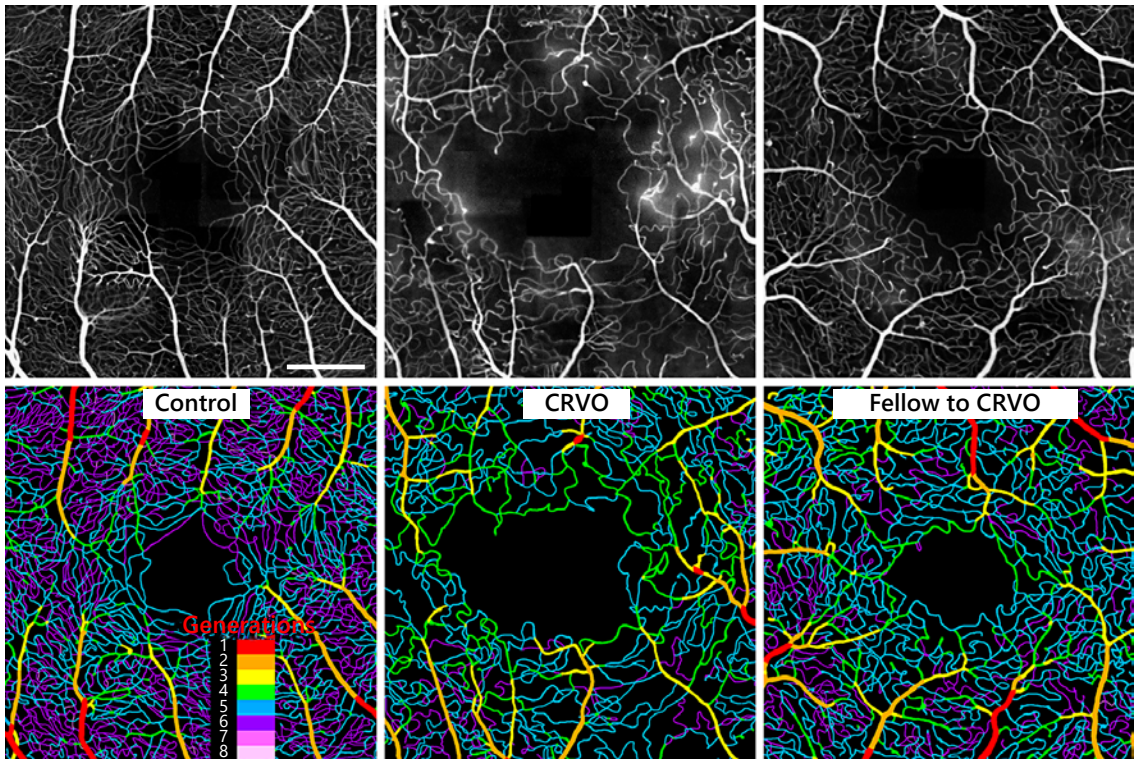

Fig. 7. Tree-network analysis of microvascular changes in the human retina from CRVO. Vessels in the parafoveal region of the human retina were imaged by AOSLO-FA [73] and analyzed by the VESGEN *Tree-Network Composite* option. Compared to the control retina of a healthy young adult, vessel density within the CRVO retina of this middle-aged subject was reduced and irregular (Table 5). Vascular damage was accompanied by prominent micro-aneurysms, considerable fluorescein leakage from the vessels, and apparent vascular dropout bordering the central avascular foveal region. Vessel changes in the fellow retina of the CRVO subject were intermediate between that of the control and CRVO. Scale bar, 300 μm. VESGEN, VESsel GENeration; CRVO, central retinal vein occlusion; AOSLO-FA, adaptive optics scanning laser ophthalmoscopy-fluorescein angiography.

and weight loss, reduced angiogenesis induced by VEGF in a mouse ear model, and reduced capillary tube formation in an endothelial cell culture model characterized by increased VEGF receptor-2 phosphorylation and activation of downstream kinases PLCγ and Erk1/2 [45]. In another study of the colonic microvascular network by VESGEN analysis [44], a statistical linkage analysis of the "open" but regular AVS was developed to further account for uniformity of the normal network compared to network disruption by DSS. In summary, vascular mapping and quantification by the *Vascular Network* option of VESGEN characterized how inflammatory angiogenesis increased vessel density and disrupted regular lattice geometry within the normal colonic microvascular network. Probiotic treatment by *S. boulardii* significantly restored the vascular network to a more normal morphology by reducing the angiogenic response.

Vascular Tree-Network Composites

Vascular Changes with CRVO in the Human Retina

As a recent revolution in ophthalmic imaging [73], adaptive optics scanning laser ophthalmoscopy-FA (AOSLO-FA) and other methods such as OCT-A can now visualize most or essentially all of the vessels within the retina (Fig. 7; Table 5). At this level of magnification, the *Tree-Network Composite* analysis option of VESGEN is appropriate because the capillaries are continuous with the precapillary arterioles and postcapillary venules. Compared to other vascular analysis software packages that analyze vascular networks (online suppl. Table 1; online suppl. methods), VESGEN additionally analyzes the branching characteristics of vascular trees. Because the 2D rendering (projection) of these retinal vascular trees that in reality are somewhat 3D results in some artifac-

Table 5. CRVO from AOSLO-FA

Parameter	Symbol	Normal retina	Fellow retina to CRVO	CRVO retina
Fractal dimension	D_f	1.629	1.568	1.521
Length density				
All vessels	L_v	174.2	111.5	89.2
Large vessels	L_{v1-3}	9.7	11.5	10.0
Small vessels	$L_{v\geq4}$	164.5	100.0	79.3
Number of AVSs		1,855	821	526
Area of AVSs	x±SD	1,352±4,712	2,555±8,311	4,495±26,132
Ratio of AVSs/ROI		0.664	0.708	0.785

Using the *Tree-Network Composite* option of VESGEN, overall vascular patterning of capillaries, arteries, and veins in a normal retina of a healthy subject and in the 2 retinas of a patient with unilateral CRVO were compared by 2 parameters, the fractal dimension (D_f) and total vessel length density (L_v). Results for vessel branching generations of 1 to 8 (G_{v1-8}) were further separated into large (G_{v1-3}) and small vessels ($G_{v\geq4}$) by the software grouping function. To examine the uniformity of the capillary network, the AVSs were calculated as mean area ±SD. Dimensions for L_v, $\times10^{-3}$ μm/μm^2 and area of AVS, μm^2; D_f, dimensionless. CRVO, central retinal vein occlusion; VESGEN, VESsel GENeration; AVS, avascular space; ROI, region of interest; AOSLO-FA, adaptive optics scanning laser ophthalmoscopy-fluorescein angiography.

tual vessel crossovers, a vascular branch point analysis is, therefore, not physically meaningful. A custom software package developed by one of us maps another important feature of connected tree-network anatomy, deviation of the capillary spatial density, and offers excellent potential for quantification of the retinal capillary density, capillary length, branch points, and end points (online suppl. Table 1; online suppl. Background) [12–14].

A normal eye of a healthy 25-year-old man served as the normal control for the eye of a patient diagnosed with CRVO and with a treatment history of multiple intravitreal bevacizumab injections (55-year-old male patient without significant past medical history), and the patient's unaffected fellow eye. The retinas were imaged by FA with AOSLO, as described previously (Fig. 7) [73], and binary (black/white) vascular patterns were extracted from the images for the VESGEN analysis.

As a consequence of occlusion of the central retinal vein, overall vascular density by D_f and L_v, together with the uniformity of the AVS, decreased considerably in the CRVO retina compared to fellow and control retinas. Results of this preliminary study indicate by all confirming measures a substantial loss of vascular space-filling capacity in the CRVO retina. As quantified by generational analysis of L_v, the major vessel loss appears to be of the more vulnerable small vessels. The area of the CRVO avascular fovea appears considerably enlarged, indicating further loss of capillaries. By D_f, L_v, and $L_{v\geq4}$, the retina of the fellow eye in this middle-aged subject displayed an intermediate status of vascular/capillary capacity compared to the normal, healthy retina of the young adult subject, as is consistent with another AOSLO-FA study on fellow eyes [74].

Vascularized Tissue-Specific 3D Bioprinting from 2D Vascular Pattern

The assignment of branch specificity to the material and cellular composition of 3D-bioprinted vascular constructs is described here as a new application of VESGEN. Generic vascular patterns have been printed before [75, 76] but without consideration to the longitudinal variations in branch composition. To illustrate the 3D printing of a vascular branching structure, a sector of an isolectin-labeled rat retina analyzed by VESGEN (Fig. 8a) was used to establish the branching generations (Fig. 8b, c) that were reduced to 3 vessel groups (large, medium, and small, Fig. 8d). The image was converted in a printable .stl (STereoLithography) format (Fig. 8e), and direct-write printed [75] with a surrogate bioink (Fig. 8f).

For this proof-of-concept application, the use of VESGEN is demonstrated by a workflow leading from a 2D vascular image to a printable vascular network with regional specificity in vascular dimensions and cellular composition. This method is currently being tested for

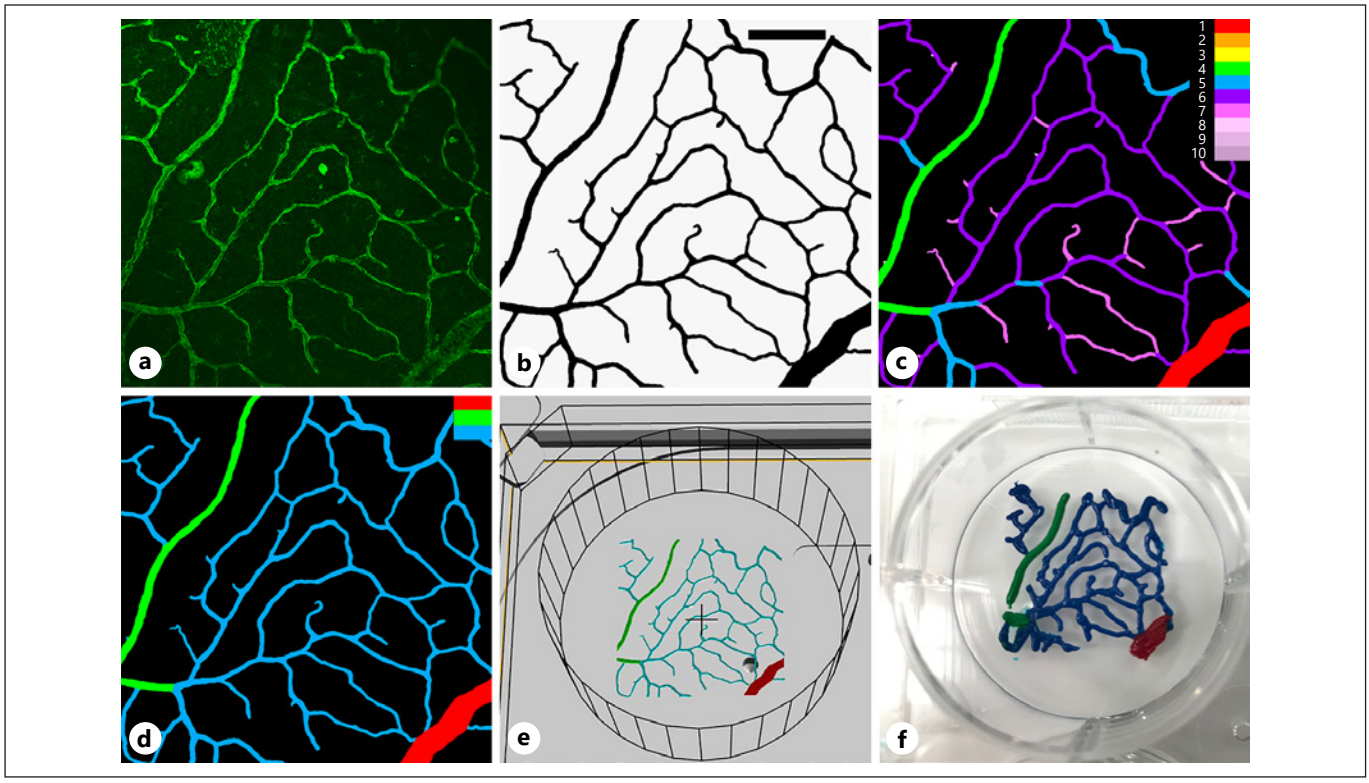

Fig. 8. Branch-specific "direct-write" 3D printing of a vascular region from a rat retina. **a** Original fluorescent image. **b** Same image after inversion, segmentation, and smoothing (scale bar, 100 μm). **c** Determination of branching generations by VESGEN (legend). By the analysis, not all branching generations were present, such as *G*2 and *G*3. **d** Same image after grouping of generation classes into large (*G*1–3, red), medium (*G*4, green), and small (*G*≥5, blue). **e** CAD conversion of the same field into a .stl printable file. **f** Direct-write printing of the vascular pattern with a bioink surrogate. VESGEN, VESsel GENeration; .stl, STereoLithography.

printing vascular constructs of the proper size in both the precapillary and capillary range, with domain-specific proportions of vascular smooth muscle and endothelial cells, embedded in bioinks with a fine-tuned composition that is adequate for the respective vascular branch (work in progress). To this end, the bioprinter's printhead will be loaded with bioinks containing different cell types and other appropriate components. For printing arterioles, for example, a higher proportion of smooth muscle cells to endothelial cells will be considered than for smaller vessels that may either lack smooth muscle cells altogether, or be replaced with pericytes.

Moreover, in addition to vascular optimization, VESGEN could further support the evolution of bioprinting from the current stage in which the bioinks are mainly generic biocompatible hydrogels such as alginate, hyaluronate, and/or gelatin [77] or fibrin [78] to the next level where the bioinks will be prepared from extracellular matrices of specific tissues or vascular beds [79]. In this context, the ability to co-register the original microvascular image with the bioprinted pattern is essential in order to apply a phenotypically matched bioink appropriate for the particular (micro)vascular branch that potentially would also contain immobilized segment-specific growth factors [80]. Such advances will be a significant technological advantage for creation of anatomically correct and physiologically relevant vascular constructs for regenerative tissue engineering.

To illustrate this new workflow, the eye of a 3-month-old male Long-Evans rat was enucleated, fixed in 4% paraformaldehyde for 24 h, stored in PBS, and the retinal flat mount dissected and immunolabeled with endothelial cell-specific Isolectin GS-IB_4 biotin conjugate (Invitrogen – I21414; Thermo Fisher Scientific, Inc., Waltham, MA, USA) and Alexa Fluor 488 (Invitrogen S-32354) according to previous methods [81]. Acquired with a Leica SP8 confocal microscope (Leica Microsystems, Wetzlar, Germany) at ×20 magnification and 2048 × 2048 pixel resolution using 488-nm excitation, the vascular image was postprocessed into a binary vascular pattern and analyzed with VESGEN using the *Vascular Tree-Network*

Composite option, as described above. A printable .stl file for 3D printing was generated using Bio-CAD software from the Bioprinting Suite of the 3DDiscovery™ bioprinter (regenHU Ltd., Switzerland). For the bioink surrogate, a glycerin-based cream (NIVEA Crème, Beiersdorf, Germany) was supplemented with commercial food dyes of red, green, and blue color to match the VESGEN-generated image.

Next, we plan to expand the branching analysis done in 2D by adding the resources of a 3D upgrade of the program to convert the linear patterns in equivalent tubular representations. The prototype for VESGEN 3D software, based in part on 3D transformations of VESGEN 2D algorithms, is being developed by NASA with new additional 3D algorithms and visualizations. The 3D software capabilities will include the conversion of a vascular 2D image into a 3D tubular vascular system that, as one example, can be used for the "blueprinting" of tissue-specific blood vessels within 3D-bioprinted tissues and organs for regeneration and replacement [27, 79]. From a stack of 2D vascular pattern images, a 3D skeleton representing the centerline of the vessels will be extracted in ImageJ. A set of branches is then derived from the 3D skeleton using an enhanced version of the AnalyzeSkeleton plugin that outputs the following attributes along the branches: branch point type (e.g., junction, slab, or end points), 3D distance map, and in the future, branching generation. To construct a 3D tube for each branch, the following steps will be performed: (1) computation of a smooth curve that interpolates the branch for (2) a set of points along the curve, constructing a circular disc, whose diameter is based on the 3D distance map value at that point, and (3) construction of 3D polygons by connecting points along the neighboring discs. After the 3D tube is constructed, the tube will be projected as a 2D image and colored by the corresponding branch generation attribute. The ultimate goal is to create a dataset with the necessary information for actual 3D bioprinting based on the initial 2D image.

Discussion

This overview of diverse in vivo and in silico models and retinal vascular diseases analyzed by VESGEN demonstrates that mapping and quantifying complex vascular patterns by algorithms specialized for the analysis of fractal branching in vascular trees, networks, and tree-network composites can yield insightful readouts and identify integrative biomarkers of multi-scale signaling for physiological, pathophysiological, and therapeutic discovery research. Vascular patterning may offer tissue-specific templates for the 3D bioprinting of regenerative tissues, organs, and replacements such as occurring in normal development. A strength of VESGEN is that the vascular analyses can be applied to any quasi-2D vascular bed imaging for support of both tissue-specific and general physiological structure-function conclusions. Other models reported elsewhere by VESGEN include infant retinopathy of prematurity in mice [5], developing and pathological coronary vessel models [5, 82], and VEGF-controlled lymphangiogenesis [21]. Globally available and freely downloadable since 2019, the software is now being used independently by other laboratories outside of NASA for studies that include tumor angiogenesis [37], human retinopathies, and 3D bioprinting.

The analysis by VESGEN is based on vertebrate vascular branching rules established by our research and others [32, 83–87]. Vertebrate vascular systems are determined by complex interactions of numerous molecular signaling cascades with hemodynamic factors and specialized tissue architectures. The vascular system is the first to develop in vertebrates, and patterns of the extracellular matrix surrounding and defining tissue-specific vascular branching may be the primary determinant of tissue-specific architecture [88]. The pro- and anti-angiogenic effects of cytokine families such as VEGF, FGF, insulin-like growth factor, and TGF-β are well established. Over 80,000 citations on VEGF alone now appear in PubMed [89]. In recent years, inflammation has received considerable attention as a unifying perspective on vascular remodeling.

Early studies with VESGEN in the avian CAM revealed that VEGF-165, bFGF, TGF-β1, angiostatin, and other regulators elicit unique "fingerprint" or "signature" vascular patterns [5, 17–19, 21–23, 45, 82]. As another optically accessible model, fluorescently labeled vascular branching in *Danio rerio* (zebra fish) would be an interesting application for the scale-invariant vascular analysis. In the CAM, for example, bFGF stimulated solely a robust dose-dependent angiogenic response [18]. However, as a novel finding facilitated by vascular mapping and quantification, VEGF induced a bimodal dose-dependent response that switched from a physiological phenotype of normal angiogenesis at low VEGF concentration to a pathological phenotype of excessive vessel dilation and leakage at high concentration that was accompanied by activation of eNOS [22]. Angiostatin inhibited angiogenesis by disrupting the vessels in a leaky, pathological fashion throughout the vascular tree [17]. In contrast, the multifunctional cytokine TGF-β1 inhibited

angiogenesis by selectively inhibiting the growth of new, small vessels while maintaining the vascular tree in a normal state [19]. The growth of new, small vessels in the CAM was also inhibited by triamcinolone acetonide, a clinical anti-inflammatory injected throughout the body, including in vitreoretinal tissue [23]. As a secondary effect, however, the steroid significantly thinned the vessels throughout generational branching of the vascular tree. Glaucoma, a major side effect of triamcinolone acetonide injection in the posterior eye, is perhaps related to the steroid's vessel thinning activity. In summary, vascular-disruptive inhibitors would seem to be the appropriate therapeutics for applications such as tumor therapy, where the goal is to destroy vessels and the diseased tissue. Vascular-preserving inhibitors, on the other hand, would be more suitable for tissues such as the inflamed retina, where the goal is to return the tissue and vessels to a healthy state.

As the most recently reported molecular "fingerprint" result, pronounced vessel tortuosity was induced by epithelial activator KGF, for which multiple effects have been demonstrated previously that include CNV [53–57]. As illustrated here for a subset of DR patients, vessel tortuosity in the body may result from the activation of KGF by molecular transduction of mechanical signaling from elevated blood pressures associated with hypertension and DR progression. Activated KGF could in turn reduce tissue stiffness by activating matrix metalloproteases. Altogether, these numerous molecular "fingerprint" results suggest that vascular patterns can serve as insightful structure-function readouts or biomarkers that help elucidate the complex, convergent molecular and mechanical signaling pathways of angiogenesis, anti-angiogenesis, and other vascular remodeling.

As discussed above, the role of cardiovascular fluid mechanics has also been studied as a causative force in microvascular patterning and remodeling [34, 51, 90]. Substantial previous research has established the contributions of blood pressure, pulsatile flow, shear stress, and cyclic shear stress to the molecular signaling of vascular response within normal, inflammatory, or other pathological contexts [91–95]. The vessel tortuosity phenotype described here of decreasing sinusoidal amplitude within a subset of DR patients and induction by epithelial activator KGF of significant vessel tortuosity further supports that signaling by pulsatile blood flow is involved in the remodeling of the vascular morphological pattern. We are often asked if VESGEN can analyze the fractal branching patterns of arterial river systems and neurons (Fig. 9) [96, 97]. Whereas river and vertebrate vascular branching

Fig. 9. Fractal patterning of self-similar branching in the aqueous transport of river systems and conduction of electrical charge in lightning. Photographs of (left) arterial river branching in the Sundarbans coast at the mouths of the Ganges emptying into the Bay of Bengal [101] and (right) lightning at night [102] illustrate the contrasting physics of self-similar fractal branching in the transport of aqueous fluids such as rivers and biological vascular systems, compared to the conduction of electricity in lightning and neuronal systems. Self-similarity is a fractal pattern whereby the characteristic pattern (in these examples, bifurcational branching) is repeated at increasingly smaller length scales. Unlike many mathematical fractals, fractals in biology and nature are irregular.

are determined by the mechanics of laminar aqueous flow, the branching of neurons appears to derive from conduction of electrical charge and, therefore, more resembles the branching patterns of lightning. Rules based on electrical signaling would, therefore, be required to develop successful branching algorithms for neuronal fractals, although basic quantification algorithms such as neuronal length density, branch points, and end points would be applicable. We can only comment that the interactive roles of cardiovascular hemodynamics and fractal vascular branching have yet to be fully defined for the determination of microvascular morphology and remodeling.

Other future advances for VESGEN software will include addition of bioinformatic dimensions to VESGEN [25, 98] by which patterns of molecular expression such as signaling receptors can be co-localized with the vascular pattern. Nonvertebrate applications of VESGEN demonstrated to date are vascular networks in genetically modified wings of *D. melanogaster* (fruit fly) [26] and the fractal scaling of developing leaves in the angiosperm *A. thaliana* (thale cress) [25]. These studies required some overriding of basic branching algorithms of VESGEN. The rules for bifurcational vascular patterning in insects and angiosperms, designed for optimal transport of vascular fluids as in vertebrates, are both similar and different from those of vertebrates. As for neuronal branching, a fully automated analysis

would require adapting the generational branching algorithms for VESGEN. Interestingly, the species-specific leaf venation patterning of angiosperms such as thale cress, maple, and oak is an accepted botanical taxonomic species identifier. Angiosperm leaf venation has sometimes been viewed as a major causative factor in the explosion in biodiversity during the Cretaceous period because of the increased efficiency in leaf photosynthesis and other vascular hydraulics compared to gymnosperms [99, 100].

In general, relatively small sample sizes have been required to achieve statistical significance for studies with VESGEN perhaps because of the large "sampling" numbers of vessels in most clinical or experimental images (such as hundreds of vessels in the human retina). However, standardization of the imaging and field of view is also very helpful [5, 17–19, 21–23, 29]. With the exception of the CAM model and perhaps the zebra fish, experimental visualization of in vivo microvasculature is difficult, requiring specialized techniques such as vascular perfusion, sophisticated immunohistochemistry, or genetic markers such as in Tie2-Cre transgenic mice. For clinical studies, the human retina is a relatively accessible site for imaging by FA or recent sophisticated methods such as OCT-A. Nonetheless, analysis by VESGEN to date has required the challenging manual segmentation (extraction) of a binary vascular pattern from microscopic or clinical images using software such as Photoshop® (Adobe) or ImageJ for accurate detection of the smaller vessels. Consequently, NASA and others are using AI/machine learning to automate vascular segmentation (VESGEN v1.11; online suppl. Table 1; online suppl. Background). Such AI segmentation is the subject of intense worldwide research for numerous vascular biomedical applications.

In conclusion, the remodeling of both normal and pathological vasculature offers an integrative, informative readout of complex molecular and other physiological signaling, when analyzed by specialized software tools such as VESGEN. Renormalization of the vasculature can be determined in part from the response of the vascular pattern to therapeutic testing. As a research discovery tool, the recently released VESGEN software has been used productively to investigate vascular remodeling in the human retina and in rodent, avian and other tissues. The vascular analysis is now being applied to the astronaut retina to help develop countermeasures for the high-priority SANS risk, thereby enabling long-duration space exploration.

Acknowledgement

The authors thank Andrew G. Farr, University of Washington, for his generous gift of recombinant KGF, and Rachel Cadle, Indiana University-Purdue University at Indianapolis, for helping with 3D image CAD conversion and printing. The opinions expressed in this report are the authors' own and do not reflect the view of NASA, the Substance Abuse and Mental Health Services Administration, the Department of Health and Human Services, or the US government.

Statement of Ethics

All images of the human retina were acquired and analyzed following approvals of study protocols at each Institutional Review Board according to the tenets of informed consent as described in Methods and additionally for NASA, by NASA's Lifetime Surveillance of Astronaut Health (LSAH). All human subjects provided informed, written consent to participate, according to the tenets of the Declaration of Helsinki. All animal studies were performed according to the Institutional Animal Care and Use Committees (IACUCs) of the various institutions.

Conflict of Interest Statement

The authors have no conflicting or competing interests to disclose.

Funding Sources

The research was supported by the US National Institutes of Health Awards R01HL110170 (MAB with PPW), R01EY027301 (TCY), DK-068181, DK-033506, AI093588, and DK-043351 (HCR); Department of Translational Hematology and Oncology Research, Cleveland Clinic Foundation (DJL); Marrus Family Foundation, New York Eye and Ear Infirmary Foundation (RBR), Indiana Institute for Medical Research and Richard L. Roudebush VA Medical Center (NM); and the National Aeronautics and Space Administration (NASA) support from the Vascularized Tissue Centennial Challenge (PPW, ML, and DK), Space Radiation Program (PPW and ML), NASA awards from STMD Game-Changing Development (PPW, HV, NO, and DK), Ames Center Innovation Fund (PPW, DK, HV, and NO), and Human Research Program by NNJ12ZSA002N (PPW, GV, GT, and SBZ) and 80NSSC19K1699 (SBZ, CAT, and PPW).

Author Contributions

All authors reviewed the paper and consented to publication. The paper was written by PPW with expert contributions by M.L., M.M., H.V., D.K., C.A.T., S.B.Z., G.T., M.B.G., D.J.L., H.C.R., A.P., T.Y.C., R.N.R., N.M., K.R., and M.B.V. Original experimental and clinical data with images and quantification,

including VESGEN analysis, were contributed by P.P.W., R.J.V., M.P., S.L., N.J., C.A.T., S.B.Z., M.B.G., M.D., D.J.L., H.C.R., A.P., T.Y.C., R.B.R., and N.M. M.L. wrote software/User Guide upgrades with consultations by D.K., H.V., M.M., M.B.V., and P.P.W. and provided expert user consultations to co-author requests for post-release beta testing. M.M., H.V., and N.O. created artificial intelligence (AI)/machine learning image analysis with consulting by M.L., D.K., and P.P.W. for the upcoming 2021 VESGEN v1.11 software release. M.B.V. and P.P.W. designed the VESGEN v1.10 analysis and algorithms described in online suppl. methods. All authors have agreed to submission and publication of the paper.

Availability of Data and Material

Availability of data and material is subject to permission by the contributing principal investigators of the various studies.

Code Availability

VESsel Generation Analysis (VESGEN) software is freely downloadable and available upon request (https://software.nasa.gov/software/ARC-17621-1) from the US National Aeronautics and Space Administration (NASA). The requester is asked to establish an external NASA identity and provide a letter of request cosigned by an administrative representative (unless the request is personal only, in which case a cosigned letter is not required).

References

1 Folkman J. Angiogenesis: an organizing principle for drug discovery? Nat Rev Drug Discov. 2007;6(4):273–86.
2 Potente M, Gerhardt H, Carmeliet P. Basic and therapeutic aspects of angiogenesis. Cell. 2011;146(6):873–87.
3 De Spiegelaere W, Casteleyn C, Van den Broeck W, Plendl J, Bahramsoltani M, Simoens P, et al. Intussusceptive angiogenesis: a biologically relevant form of angiogenesis. J Vasc Res. 2012;49(5):390–404.
4 Martin JD, Duda DG, Jain RK. Going beyond VEGF Pathway inhibition for antiangiogenic cancer therapy: is inhibition of the PP2A/B55alpha complex the answer? Circ Res. 2020;127(6):724–6.
5 Vickerman MB, Keith PA, McKay TL, Gedeon DJ, Watanabe M, Montano M, et al. VESGEN 2D: automated, user-interactive software for quantification and mapping of angiogenic and lymphangiogenic trees and networks. Anat Rec. 2009;292(3):320–32.
6 Corliss BA, Doty RW, Mathews C, Yates PA, Zhang T, Peirce SM. REAVER: a program for improved analysis of high-resolution vascular network images. Microcirculation. 2020;27(5):e12618.
7 Montoya-Zegarra JA, Russo E, Runge P, Jadhav M, Willrodt AH, Stoma S, et al. AutoTube: a novel software for the automated morphometric analysis of vascular networks in tissues. Angiogenesis. 2019;22(2):223–36.
8 Zudaire E, Gambardella L, Kurcz C, Vermeren S. A computational tool for quantitative analysis of vascular networks. PLoS One. 2011;6(11):e27385.
9 Cheung CY, Xu D, Cheng CY, Sabanayagam C, Tham YC, Yu M, et al. A deep-learning system for the assessment of cardiovascular disease risk via the measurement of retinal-vessel calibre. Nat Biomed Eng. 2020.
10 McGrory S, Taylor AM, Pellegrini E, Ballerini L, Kirin M, Doubal FN, et al. Towards standardization of quantitative retinal vascular parameters: comparison of SIVA and VAMPIRE measurements in the Lothian Birth Cohort 1936. Transl Vis Sci Technol. 2018;7(2):12.
11 Yip W, Tham YC, Hsu W, Lee ML, Klein R, Klein B, et al. Comparison of common retinal vessel caliber measurement software and a conversion algorithm. Transl Vis Sci Technol. 2016;5(5):11.
12 Mo S, Phillips E, Krawitz BD, Garg R, Salim S, Geyman LS, et al. Visualization of radial peripapillary capillaries using optical coherence tomography angiography: the effect of image averaging. PLoS One. 2017;12(1):e0169385.
13 Pinhas A, Linderman R, Mo S, Krawitz BD, Geyman LS, Carroll J, et al. A method for age-matched OCT angiography deviation mapping in the assessment of disease- related changes to the radial peripapillary capillaries. PLoS One. 2018;13(5):e0197062.
14 Andrade Romo JS, Linderman RE, Pinhas A, Carroll J, Rosen RB, Chui TYP. Novel development of parafoveal capillary density deviation mapping using an age-group and eccentricity matched normative OCT angiography database. Transl Vis Sci Technol. 2019;8(3):1.
15 Todorov MI, Paetzold JC, Schoppe O, Tetteh G, Shit S, Efremov V, et al. Machine learning analysis of whole mouse brain vasculature. Nat Methods. 2020;17(4):442–9.
16 Niemisto A, Dunmire V, Yli-Harja O, Zhang W, Shmulevich I. Robust quantification of in vitro angiogenesis through image analysis. IEEE Trans Med Imaging. 2005;24(4):549–53.
17 Parsons-Wingerter P, Lwai B, Yang MC, Elliott KE, Milaninia A, Redlitz A, et al. A novel assay of angiogenesis in the quail chorioallantoic membrane: stimulation by bFGF and inhibition by angiostatin according to fractal dimension and grid intersection. Microvasc Res. 1998;55(3):201–14.
18 Parsons-Wingerter P, Elliott KE, Clark JI, Farr AG. Fibroblast growth factor-2 selectively stimulates angiogenesis of small vessels in arterial tree. Arterioscler Thromb Vasc Biol. 2000;20(5):1250–6.
19 Parsons-Wingerter P, Elliott KE, Farr AG, Radhakrishnan K, Clark JI, Sage EH. Generational analysis reveals that TGF-beta1 inhibits the rate of angiogenesis in vivo by selective decrease in the number of new vessels. Microvasc Res. 2000;59(2):221–32.
20 Lazarovici P, Gazit A, Staniszewska I, Marcinkiewicz C, Lelkes PI. Nerve growth factor (NGF) promotes angiogenesis in the quail chorioallantoic membrane. Endothelium. 2006;13(1):51–9.
21 Parsons-Wingerter P, McKay TL, Leontiev D, Vickerman MB, Condrich TK, Dicorleto PE. Lymphangiogenesis by blind-ended vessel sprouting is concurrent with hemangiogenesis by vascular splitting. Anat Rec A Discov Mol Cell Evol Biol. 2006;288(3):233–47.
22 Parsons-Wingerter P, Chandrasekharan UM, McKay TL, Radhakrishnan K, DiCorleto PE, Albarran B, et al. A VEGF165-induced phenotypic switch from increased vessel density to increased vessel diameter and increased endothelial NOS activity. Microvasc Res. 2006;72(3):91–100.
23 McKay TL, Gedeon DJ, Vickerman MB, Hylton AG, Ribita D, Olar HH, et al. Selective inhibition of angiogenesis in small blood vessels and decrease in vessel diameter throughout the vascular tree by triamcinolone acetonide. Invest Ophthalmol Vis Sci. 2008;49(3):1184–90.
24 Lazarovici P, Lahiani A, Gincberg G, Haham D, Marcinkiewicz C, Lelkes PI. Nerve growth factor-induced angiogenesis: 2. the quail chorioallantoic membrane assay. Methods Mol Biol. 2018;1727:251–9.
25 Parsons-Wingerter P, Vickerman MB, Paul AL, Ferl RJ. Mapping by VESGEN of leaf venation patterning in Arabidopsis thaliana with bioinformatic dimensions of gene expression. Grav Space Res. 2014;2(1):68–81.
26 Parsons-Wingerter P, Hosamani R, Vickerman MB, Bhattacharya S. Mapping by VESGEN of wing vein phenotype in drosophila for quantifying adaptations to space environments. Grav Space Res. 2015;3(2):54–64.

27 Vessel Generation Analysis (VESGEN) 2D Software U.S. National Aeronautics and Space Administration. Available from: https://software.nasa.gov/software/ARC-17621-1.
28 ImageJ, U.S. National Institutes of Health. Available from: https://imagej.nih.gov/ij/download.html.
29 Avakian A, Kalina RE, Sage EH, Rambhia AH, Elliott KE, Chuang EL, et al. Fractal analysis of region-based vascular change in the normal and non-proliferative diabetic retina. Curr Eye Res. 2002;24(4):274–80.
30 Vyas RJ, Young M, Murray MC, Predovic M, Lim S, Mason SS, et al. Decreased retinal vascular patterning in ISS crew members as new measure and of ocular damage in SANS. Invest Ophthalmol Vis Sci. 2020;61(14):34.
31 Mandelbrot BB. The fractal geometry of nature. San Francisco: W. H. Freeman; 1983.
32 Bassingthwaighte JB, Liebovitch LS, West BJ. Fractal physiology. The American Physiological Society Methods in physiology series. New York: Oxford University Press; 1994.
33 Han HC. Twisted blood vessels: symptoms, etiology and biomechanical mechanisms. J Vasc Res. 2012;49(3):185–97.
34 Kalitzeos AA, Lip GY, Heitmar R. Retinal vessel tortuosity measures and their applications. Exp Eye Res. 2013;106:40–6.
35 Appaji A, Nagendra B, Chako DM, Padmanabha A, Jacob A, Hiremath CV, et al. Retinal vascular tortuosity in schizophrenia and bipolar disorder. Schizophr Res. 2019;212:26–32.
36 Parsons-Wingerter P, Radhakrishnan K, Vickerman MB, Kaiser PK. Oscillation of angiogenesis with vascular dropout in diabetic retinopathy by VESsel GENeration analysis (VESGEN). Invest Ophthalmol Vis Sci. 2010;51(1):498–507.
37 Zamanian-Daryoush M, Lindner D, Tallant TC, Wang Z, Buffa J, Klipfell E, et al. The cardioprotective protein apolipoprotein A1 promotes potent anti-tumorigenic effects. J Biol Chem. 2013;288(29):21237–52.
38 LaRue AC, Mironov VA, Argraves WS, Czirók A, Fleming PA, Drake CJ. Patterning of embryonic blood vessels. Dev Dyn. 2003;228(1):21–9.
39 Liskowski P, Krawiec K. Segmenting retinal blood vessels with deep neural networks. IEEE Trans Med Imaging. 2016;35(11):2369–80.
40 DRIVE: Digital Retinal Images for Vessel Extraction. Available from: https://drive.grand-challenge.org.
41 Mader TH, Gibson CR, Pass AF, Kramer LA, Lee AG, Fogarty J, et al. Optic disc edema, globe flattening, choroidal folds, and hyperopic shifts observed in astronauts after long-duration space flight. Ophthalmology. 2011;118(10):2058–69.
42 Spaceflight-Associated Neuro-ocular Syndrome (SANS) HRP, U.S. National Aeronautics and Space Administration. Available from: https://humanresearchroadmap.nasa.gov/Risks/risk.aspx?i=105.
43 Zhang LF, Hargens AR. Spaceflight-induced intracranial hypertension and visual impairment: pathophysiology and countermeasures. Physiol Rev. 2018;98(1):59–87.
44 Parsons-Wingerter P, Reinecker HC. For application to human spaceflight and ISS experiments: VESGEN mapping of microvascular network remodeling during intestinal inflammation. Gravit Space Biol Bull. 2012;26(2):2–12.
45 Chen X, Yang G, Song JH, Xu H, Li D, Goldsmith J, et al. Probiotic yeast inhibits VEGFR signaling and angiogenesis in intestinal inflammation. PLoS One. 2013;8(5):e64227.
46 U.S. Centers for Disease Control and Prevention. Available from: https://www.cdc.gov/visionhealth/basics/ced/index.html
47 Jarajapu YP, Bhatwadekar AD, Caballero S, Hazra S, Shenoy V, Medina R, et al. Activation of the ACE2/angiotensin-(1-7)/Mas receptor axis enhances the reparative function of dysfunctional diabetic endothelial progenitors. Diabetes. 2013;62(4):1258–69.
48 Dominguez JM 2nd, Hu P, Caballero S, Moldovan L, Verma A, Oudit GY, et al. Adeno-associated virus overexpression of angiotensin-converting enzyme-2 reverses diabetic retinopathy in type 1 diabetes in mice. Am J Pathol. 2016;186(6):1688–700.
49 Duan Y, Beli E, Li Calzi S, Quigley JL, Miller RC, Moldovan L, et al. Loss of angiotensin-converting enzyme 2 exacerbates diabetic retinopathy by promoting bone marrow dysfunction. Stem Cells. 2018;36(9):1430–40.
50 Duan Y, Prasad R, Feng D, Beli E, Li Calzi S, Longhini ALF, et al. Bone marrow-derived cells restore functional integrity of the gut epithelial and vascular barriers in a model of diabetes and ACE2 deficiency. Circ Res. 2019;125(11):969–88.
51 Ramos L, Novo J, Rouco J, Romeo S, Álvarez MD, Ortega M. Retinal vascular tortuosity assessment: inter-intra expert analysis and correlation with computational measurements. BMC Med Res Methodol. 2018;18(1):144.
52 Cabrera DeBuc D, Somfai GM, Arthur E, Kostic M, Oropesa S, Mendoza Santiesteban C. Investigating multimodal diagnostic eye biomarkers of cognitive impairment by measuring vascular and neurogenic changes in the retina. Front Physiol. 2018;9:1721.
53 Finch PW, Rubin JS. Keratinocyte growth factor/fibroblast growth factor 7, a homeostatic factor with therapeutic potential for epithelial protection and repair. Adv Cancer Res. 2004;91:69–136.
54 Toriseva M, Ala-aho R, Peltonen S, Peltonen J, Grénman R, Kähäri VM. Keratinocyte growth factor induces gene expression signature associated with suppression of malignant phenotype of cutaneous squamous carcinoma cells. PLoS One. 2012;7(3):e33041.
55 Braun S, Krampert M, Bodó E, Kümin A, Born-Berclaz C, Paus R, et al. Keratinocyte growth factor protects epidermis and hair follicles from cell death induced by UV irradiation, chemotherapeutic or cytotoxic agents. J Cell Sci. 2006;119(Pt 23):4841–9.
56 Zhang C, Han M, Wu S. Silencing fibroblast growth factor 7 inhibits krypton laser-induced choroidal neovascularization in a rat model. J Cell Biochem. 2019;120(8):13792–801.
57 Niu J, Chang Z, Peng B, Xia Q, Lu W, Huang P, et al. Keratinocyte growth factor/fibroblast growth factor-7-regulated cell migration and invasion through activation of NF-kappaB transcription factors. J Biol Chem. 2007;282(9):6001–11.
58 Erickson M, Morkowski S, Lehar S, Gillard G, Beers C, Dooley J, et al. Regulation of thymic epithelium by keratinocyte growth factor. Blood. 2002;100(9):3269–78.
59 Bielenberg DR, Zetter BR. The contribution of angiogenesis to the process of metastasis. Cancer J. 2015;21(4):267–73.
60 Burger DR, Parker Y, Guinta K, Lindner D. PRO 140 monoclonal antibody to CCR5 prevents acute xenogeneic graft-versus-host disease in NOD-scid IL-2Ry(null) mice. Biol Blood Marrow Transplant. 2018;24(2):260–6.
61 Velasco-Velazquez M, Jiao X, De La Fuente M, Pestell TG, Ertel A, Lisanti MP, et al. CCR5 antagonist blocks metastasis of basal breast cancer cells. Cancer Res. 2012;72(15):3839–50.
62 Sicoli D, Jiao X, Ju X, Velasco-Velazquez M, Ertel A, Addya S, et al. CCR5 receptor antagonists block metastasis to bone of v-Src oncogene-transformed metastatic prostate cancer cell lines. Cancer Res. 2014;74(23):7103–14.
63 Soria G, Ben-Baruch A. The inflammatory chemokines CCL2 and CCL5 in breast cancer. Cancer Lett. 2008;267(2):271–85.
64 Ben-Baruch A. The tumor-promoting flow of cells into, within and out of the tumor site: regulation by the inflammatory axis of TNFalpha and chemokines. Cancer Microenviron. 2012;5(2):151–64.
65 Riesner K, Shi Y, Jacobi A, Kräter M, Kalupa M, McGearey A, et al. Initiation of acute graft-versus-host disease by angiogenesis. Blood. 2017;129(14):2021–32.
66 Danese S, Sans M, Spencer DM, Beck I, Dońate F, Plunkett ML, et al. Angiogenesis blockade as a new therapeutic approach to experimental colitis. Gut. 2007;56(6):855–62.
67 Alkim C, Alkim H, Koksal AR, Boga S, Sen I. Angiogenesis in inflammatory bowel disease. Int J Inflam. 2015;2015:970890.
68 Chidlow JH Jr, Shukla D, Grisham MB, Kevil CG. Pathogenic angiogenesis in IBD and experimental colitis: new ideas and therapeutic avenues. Am J Physiol Gastrointest Liver Physiol. 2007;293(1):G5–18.
69 Scaldaferri F, Vetrano S, Sans M, Arena V, Straface G, Stigliano E, et al. VEGF-A links angiogenesis and inflammation in inflammatory bowel disease pathogenesis. Gastroenterology. 2009;136(2):585–e5.
70 Floch MH, Walker WA, Sanders ME, Nieuwdorp M, Kim AS, Brenner DA, et al. Recommendations for probiotic use: 2015 update: proceedings and consensus opinion. J Clin Gastroenterol. 2015;49(Suppl 1):S69–73.

71 Stier H, Bischoff SC. Saccharomyces boulardii CNCM I-745 influences the gut-associated immune system. MMW Fortschr Med. 2017; 159(Suppl 5):1–6.
72 Konerding MA, Fait E, Gaumann A. 3D microvascular architecture of pre-cancerous lesions and invasive carcinomas of the colon. Br J Cancer. 2001;84(10):1354–62.
73 Pinhas A, Dubow M, Shah N, Chui TY, Scoles D, Sulai YN, et al. In vivo imaging of human retinal microvasculature using adaptive optics scanning light ophthalmoscope fluorescein angiography. Biomed Opt Express. 2013; 4(8):1305–17.
74 Pinhas A, Dubow M, Shah N, Cheang E, Liu CL, Razeen M, et al. Fellow eye changes in patients with nonischemic central retinal vein occlusion: assessment of perfused foveal microvascular density and identification of nonperfused capillaries. Retina. 2015;35(10): 2028–36.
75 Smith CM, Stone AL, Parkhill RL, Stewart RL, Simpkins MW, Kachurin AM, et al. Three-dimensional bioassembly tool for generating viable tissue-engineered constructs. Tissue Eng. 2004;10(9–10):1566–76.
76 Lee A, Hudson AR, Shiwarski DJ, Tashman JW, Hinton TJ, Yerneni S, et al. 3D bioprinting of collagen to rebuild components of the human heart. Science. 2019;365(6452):482–7.
77 Axpe E, Oyen ML. Applications of alginate-based bioinks in 3D bioprinting. Int J Mol Sci. 2016;17(12):1976.
78 Nakamura M, Iwanaga S, Henmi C, Arai K, Nishiyama Y. Biomatrices and biomaterials for future developments of bioprinting and biofabrication. Biofabrication. 2010;2(1): 014110.
79 Kim BS, Kim H, Gao G, Jang J, Cho DW. Decellularized extracellular matrix: a step towards the next generation source for bioink manufacturing. Biofabrication. 2017;9(3): 034104.
80 Buschmann I, Heil M, Jost M, Schaper W. Influence of inflammatory cytokines on arteriogenesis. Microcirculation. 2003;10(3–4):371–9.
81 Tual-Chalot S, Allinson KR, Fruttiger M, Arthur HM. Whole mount immunofluorescent staining of the neonatal mouse retina to investigate angiogenesis in vivo. J Vis Exp. 2013; 77(77):e50546.
82 Liu H, Yang Q, Radhakrishnan K, Whitfield DE, Everhart CL, Parsons-Wingerter P, et al. Role of VEGF and tissue hypoxia in patterning of neural and vascular cells recruited to the embryonic heart. Dev Dyn. 2009;238(11): 2760–9.
83 Gan RZ, Tian Y, Yen RT, Kassab GS. Morphometry of the dog pulmonary venous tree. J Appl Physiol. 1993;75(1):432–40.
84 Kalsho G, Kassab GS. Bifurcation asymmetry of the porcine coronary vasculature and its implications on coronary flow heterogeneity. Am J Physiol Heart Circ Physiol. 2004;287(6): H2493–500.
85 Kassab GS, Lin DH, Fung YC. Morphometry of pig coronary venous system. Am J Physiol. 1994;267(6 Pt 2):H2100–13.
86 Kassab GS, Rider CA, Tang NJ, Fung YC. Morphometry of pig coronary arterial trees. Am J Physiol. 1993;265(1 Pt 2):H350–65.
87 Hall JE. Guyton and hall textbook of medical physiology, vol chapter 16. The microcirculation and lymphatic system: capillary fluid exchange, interstitial fluid, and lymph flow. 13th ed. Philadelphia PA: Elsevier; 2016.
88 Ott HC, Matthiesen TS, Goh SK, Black LD, Kren SM, Netoff TI, et al. Perfusion-decellularized matrix: using nature's platform to engineer a bioartificial heart. Nat Med. 2008; 14(2):213–21.
89 PubMED, U. S. National Institutes of Health. Available from: https://pubmed.ncbi.nlm.nih.gov/?term=VEGF.
90 Lehoux S, Jones EA. Shear stress, arterial identity and atherosclerosis. Thromb Haemost. 2016;115(3):467–73.
91 Reinhart-King CA, Fujiwara K, Berk BC. Physiologic stress-mediated signaling in the endothelium. Meth Enzymol. 2008;443:25–44.
92 Wang Z, Wang F, Kong X, Gao X, Gu Y, Zhang J. Oscillatory shear stress induces oxidative stress via TLR4 activation in endothelial cells. Mediators Inflamm. 2019;2019: 7162976.
93 Zhou J, Li YS, Chien S. Shear stress-initiated signaling and its regulation of endothelial function. Arterioscler Thromb Vasc Biol. 2014;34(10):2191–8.
94 Marin T, Gongol B, Chen Z, Woo B, Subramaniam S, Chien S, et al. Mechanosensitive microRNAs-role in endothelial responses to shear stress and redox state. Free Radic Biol Med. 2013;64:61–8.
95 Chistiakov DA, Orekhov AN, Bobryshev YV. Effects of shear stress on endothelial cells: go with the flow. Acta Physiol. 2017; 219(2):382–408.
96 Lee WC, Huang H, Feng G, Sanes JR, Brown EN, So PT, et al. Dynamic remodeling of dendritic arbors in GABAergic interneurons of adult visual cortex. PLoS Biol. 2006;4(2): e29.
97 Peng H, Zhou Z, Meijering E, Zhao T, Ascoli GA, Hawrylycz M. Automatic tracing of ultra-volumes of neuronal images. Nat Methods. 2017;14(4):332–3.
98 Parsons-Wingerter P, Vickerman MB. U.S. Patent 10,282,841. Bioinformatic analysis of vascular patterning. 2019.
99 Boyce CK, Brodribb TJ, Feild TS, Zwieniecki MA. Angiosperm leaf vein evolution was physiologically and environmentally transformative. Proc Biol Sci. 2009;276(1663): 1771–6.
100 Brodribb TJ, Feild TS. Leaf hydraulic evolution led a surge in leaf photosynthetic capacity during early angiosperm diversification. Ecol Lett. 2010;13(2):175–83.
101 Sundarbans coast, Bay of Bengal. U.S. National Aeronautics and Space Administration. Available from: https://earthobservatory.nasa.gov/images/7028/sundarbans-bangladesh.
102 Lightning. U.S. National Oceanic and Atmospheric Administration. Available from: https://www.google.com/search?rls=en&sxsrf=ACYBGNQ7aS1BMdLQjycTmic14bwgElst9g:1575841670489&q=NOAA+Lightning+Ls+0016&tbm=isch&source=univ&client=safari&sa=X&ved=2ahUKEwiylffXg6fmAhXKzlkKHVaGBAoQsAR6BAgKEAE&biw=1423&bih=1185